Combined PARP14 Inhibition and PD-1 Blockade Promotes Cytotoxic T Cell Quiescence and Modulates Macrophage Polarisation in Relapsed Melanoma

Rotem Leshem[1,2,$], Kieran N. Sefton[1,2,$], Chun Wai Wong[1,2,3,4], I-Hsuan Lin[5], Dervla T. Isaac[6], Mario Niepel[6], and Adam F.L. Hurlstone[1,2,#]

[1]School of Biological Sciences, Faculty of Biology, Medicine and Health, The University of Manchester, Manchester, M13 9PT, UK

[2]Lydia Becker Institute of Immunology, The University of Manchester, Manchester, M13 9PT, UK

[3]Now at Massachusetts General Hospital Cancer Center, Department of Medicine, Massachusetts General Hospital, Harvard Medical School, Boston, MA, USA

[4]Now at Broad Institute of MIT and Harvard, Cambridge, MA, USA

[5]Bioinformatics Core Facility, The University of Manchester, Manchester, M13 9PT, UK

[6]Ribon Therapeutics Inc., 35 Cambridge Park Drive, Suite 300, Cambridge, MA 02140, USA

[$]These authors contributed equally

[#]To whom correspondence should be addressed: Dr Adam Hurlstone, Michael Smith Building, The University of Manchester, Dover Street, Manchester M13 9PT, UK; tel: +44 161 2751574; email: adam.hurlstone@manchester.ac.uk

Abstract

Programmed Cell Death 1 (PD-1) signalling blockade is effective in restoring immune surveillance and treating melanoma. However, immune homeostatic mechanisms driven by chronic interferon-gamma (IFNγ) signalling in melanoma cells reduce efficacy, leading to persistent immune evasion and the development of acquired treatment resistance. Previously, we demonstrated that poly ADP ribosyl polymerase 14 (PARP14), encoded by an IFNγ-responsive gene, mediates IFNγ-driven resistance, as inhibition of PARP14 prolonged responsiveness to PD-1 blockade in preclinical models. Nevertheless, inhibition of PARP14 alone was insufficient to fully restore immune clearance, suggesting the presence of redundant resistance mechanisms. The findings here reveal a robust PARP14 catalytic inhibitor (PARP14i) gene signature associated with improved patient survival. We further elucidate the response and adaptation of the immune infiltrate and melanoma cells to PARP14 inhibition using preclinical models. Combining PARP14i with PD-1 blockade therapy revitalised cytotoxic T cells, driving them into a quiescent state while reducing alternatively activated macrophages and increasing pro-inflammatory memory macrophages. Despite this initial enhancement of immune responses through combination therapy, adaptive resistance mechanisms emerged within tumour cells, engaging alternative exhaustion pathways. Our findings indicate that this novel combination therapy leaves immune cells primed for further therapeutic intervention, offering a strategy to address resistance development and optimise treatment outcomes comprehensively.

Keywords: PARP14, T cell exhaustion, quiescent T cells, memory macrophages, adaptive resistance

Introduction

Nivolumab and pembrolizumab, drugs antagonising the PD-1 signalling axis by interfering with PD-1's interaction with Programmed Cell Death Ligand 1 (PD-L1) on exhausted T cells, have vastly improved outcomes for patients with high-risk and late-stage melanoma. However, among responders to PD-1 blockade therapy, approximately 25% will relapse within two years of initiating treatment [1]. Little can be done at present for these patients. Analysis of relapsing tumours has revealed that 30% are characterised by intrinsic—that is, ligand-independent—IFNγ signalling [2]. Intrinsic IFNγ signalling in cancer cells has been shown to follow chronic IFNγ stimulation and to entail epigenetic remodelling wherein signal transducer and activator of transcription 1 (STAT1) and Interferon Regulatory Factor 3 (IRF3) permanently occupy the regulatory sites of a subset of interferon-stimulated genes (ISG), including notably those promoting T cell dysfunction [3]. Indeed, the ISG selectively upregulated in chronically stimulated cancer cells (ISG resistance signature or ISG.RS) predicts poor survival in patients and poor response to PD-1 blockade [4].

Our previous work revealed a contribution from PARP14 in mediating the ability of chronic IFNγ stimulation to drive PD-1 blockade resistance in preclinical models [5]. One model we developed entailed implantation of the mouse rapidly accelerated fibrosarcoma homolog B (BRAF) and Phosphatase and tensin homolog (PTEN) mutant melanoma cell line YUMM2.1 [6] into the hypodermis of syngeneic C57/BL6 mice, and then treating these mice with a short course of anti-PD-1 (α-PD-1) antibodies when tumours became palpable. In tumours that resumed growth following α-PD-1 treatment, we observed increased expression of multiple ISG, including ISG.RS genes, relative to control (untreated) tumours and to tumours still responding to PD-1 blockade therapy [5]. AI-assisted immune profiling, based on

deconvolving gene expression, indicated that relapsing tumours were also relatively more T cell infiltrated, including by T_{EM} and $T_{CM.}$ However, T cells were also more dysfunctional compared to these other two tumour groups [5]. The regrowth of such tumours was significantly delayed—but not abolished— and survival lengthened by adding a highly potent and selective PARP14 inhibitor RBN012759 (PARP14i, Ribon Therapeutics)[7] to the treatment regime [5].

This previous study also highlighted that the gene encoding PARP14 is a STAT1 target and that PARP14 itself is a STAT1 interacting protein [5]. Moreover, in macrophages, PARP14 interaction with STAT1 inhibits the expression of proinflammatory genes [8] but regulates IRF3 recruitment of RNA polII to promoters of IRF3 target genes [9] and is thus positioned to influence the expression of ISG. However, the details are far from clear. Certainly, our previous analysis of gene expression indicated that PARP14 inhibitor treatment of melanoma cells chronically stimulated with IFNγ increased IFN-, TNF-α-, and IL-6-driven inflammatory signalling [5].

Intrigued by the potential of PARP14 to influence the expression of ISG in tumour cells but also the failure of PARP14 inhibitor treatment to permanently flatten tumour rebound after α-PD-1 treatment, we undertook a detailed analysis of tumour composition and gene expression changes attending PARP14 inhibitor treatment to identify other targets for intervention which we now present below.

Materials and Methods

Reagents

Recombinant human IFNγ (PHC4031, Gibco) and recombinant mouse IFNγ (PMC4031, Gibco). PARP14 inhibitor RBN012759 [7] and PARP14 PROTAC RBN012811 (Ribon Therapeutics) [10].

Cell lines

Human melanoma cell lines A375 and 501-Mel (provided by Claudia Wellbrock, The University of Manchester), MC38 cells (provided by Santiago Zelenay, The University of Manchester) and YUMM2.1 cells (provided by Richard Marais, The University of Manchester) were maintained in RPMI-1640 (Sigma–Aldrich) supplemented with 10% v/v foetal bovine serum (Life Technologies) and 1% w/v penicillin-streptomycin (Sigma–Aldrich), at 37 °C in a 5% v/v CO_2 humidified incubator. Cell lines authenticated by STR profiling; cultures routinely tested for mycoplasma. Cells were treated for two weeks with 50 IU/mL IFNγ, refreshed every 2-3 days, and subsequently treated with 500nM DMSO (Sigma–Aldrich); 500nM PARP14i; or 100nM PARP14 PROTAC for 48h.

Mouse tumour implants

Mice were housed in the Biological Services Facility of The University of Manchester on a 12/12 h light/dark cycle and given ad libitum food (Bekay, B&K Universal, Hull, UK) and water. All procedures were approved by the University of Manchester's animal welfare ethical review board and performed under relevant Home Office licences according to the UK Animals (Scientific Procedures) Act, 1986.

8–12-week-old C57BL/6 female mice (ENVIGO) were allowed 1-week to acclimatise. YUMM2.1 cells (5×10^6 cells) in 100 µL serum-free RPMI-1640 were subcutaneously injected into the left flank. Tumour volumes (height x width x length calliper measurements) and

120 mouse weights were monitored every 2–3 days. When tumours reached a volume of 80
121 mm^3, mice were administered two doses of 300 µg α-PD-1 antibody (BioXCell) in 100 µL
122 InVivoPure pH 7.0 Dilution Buffer (BioXCell) via intraperitoneal (i.p.) injection administered
123 at 3-day intervals. Mice were culled if tumours remained under 100 mm^3 (total responders)
124 or conversely reached 800 mm3 (non-responders). Otherwise, mice with tumours recovering
125 to 140 mm^3 were randomised on to a second round of treatments (re-treatment): 2 doses of
126 300 µg of rat isotype control antibody IgG2b (BioXCell) (IgG group) or α-PD-1 antibody
127 (BioXCell) (α-PD-1 group) in 100 µL InVivoPure pH 7.0 Dilution Buffer (BioXCell) via i.p.
128 injection at three-day intervals, 14 doses of 500 mg/Kg of PARP14I by oral gavage twice a day
129 (PARP14i group), or a combination of α-PD-1 i.p. and PARP14i gavage in the same doses
130 (Combination group). PARP14i was dissolved in 0.5% w/v methylcellulose (Sigma–Aldrich) +
131 0.2% v/v Tween 80 (Sigma–Aldrich). Dose volume - 10 mL/kg.

132 **Tumour immune infiltrate analysis by flow cytometry**

133 Tumours were dissected upon reaching 250-400mm^3 following retreatment and incubated
134 for 45 minutes with 100 µg/mL Liberase (Sigma–Aldrich) in serum-free media at 37 °C, then
135 pushed through a 100 µM nylon cell strainer. The cell suspension was stained for 20 min
136 with Zombie UV™ Fixable Viability Kit (BioLegend) in PBS. Subsequently, Fc receptors were
137 blocked, and cells were stained with a surface stain antibody mix. Cells were fixed and
138 permeabilised using the Foxp3/Transcription Factor Staining Buffer Set (eBioscience)
139 following manufacturer instructions. Samples were measured on a BD Fortessa flow
140 cytometer (BDBiosciences), and data was collected using BD FACSDiva™ software. For all
141 antibodies, a non-stained cell sample and appropriate fluorescence minus one control were
142 analysed as well. Data were analysed using FlowJo version 8.7.

143 Antibodies: CD16/32 (clone 93), CD45 (Cat. 103132), CD3ε (Cat. 100306), CD4 (Cat. 100552),
144 CD8α (Cat. 100742), PD-1 (Cat. 135231), LAG-3 (Cat. 125224), TIM-3 (Cat. 119721), Ki-67
145 (Cat. 652420), Granzyme B (Cat. 372214), CD69 (Cat. 104531), and CTLA-4 (Cat. 106338)
146 from Biolegend. Tox (Cat. 12-6502-82) was purchased from eBioscience. Gating strategy as
147 described in SUPPLEMENTARY FIGURE 5.

148 **Single-cell RNAseq sequencing**

149 **Tumour processing**

150 Tumours were collected on day 7 of retreatment into serum-free RPMI on ice, then minced
151 into 1mm pieces and incubated at 37 °C up to 60 min in Liberase TL (Millipore Sigma) with
152 rocking according to manufacturer instructions. Digestion was stopped using foetal bovine
153 serum, and tissue was further dissociated using a wide-bore pipette and filtered through a
154 cell strainer to achieve a single-cell solution. Immune population enrichment was done by
155 CD45 mouse Microbeads (Miltenyi) according to manufacturer instructions. Following
156 sorting, both populations were counted, and ~5% of CD45 negative cells were spiked back
157 into the CD45 positive fraction.

158 Cells were fixed for 18 hours, then quenched and stored at -80°C in Enhancer according to
159 10x Genomics Tissue Fixation & Dissociation for Chromium Fixed RNA Profiling protocol
160 (CG000553 Rev A) until all samples were collected.

161 **Single-cell isolation and library construction**

162 Gene expression libraries were prepared from formaldehyde-fixed samples using the
163 Chromium X and Chromium Fixed RNA kit, Mouse Transcriptome, 4 rxns x 16 BC (10x
164 Genomics, Inc.) according to the manufacturer's protocol (CG000527 Rev C).

Illumina-compatible sequencing libraries were constructed by adding P5, P7, i5 and i7 sample indexes and Illumina Small Read 2 sequences to the 10x barcoded, ligated probe products via Sample Index PCR followed by a SPRIselect size-selection.

Sequencing

The resulting sequencing library comprised standard Illumina paired-end constructs flanked with P5 and P7 sequences. The 16 bp 10x Barcode and 12 bp UMI were encoded in Read 1, while Read 2 sequenced the ligated probe insert, constant sequence and the 8bp Probe Barcode. Sample indexes were incorporated as the i5 and i7 index reads. Paired-end sequencing (28:90) was performed on the Illumina NovaSeq6000 platform.

Data Analysis

Raw data processing and cell filtering

Raw sequencing data were processed using the 10x Genomics Cell Ranger pipeline (v7.0.0). Base call (BCL) files generated by the sequencer were demultiplexed and converted to FASTQ files using “cellranger mkfastq”. The FASTQ files were then mapped against the pre-built Mouse reference package from 10X Genomics (mm10-2020-A) using “cellranger multi” to demultiplex and produce the gene-cell barcode matr-ix for individual samples.

The single-cell data were processed in R environment (v4.1) following the workflow documented in Orchestrating Single-Cell Analysis with Bioconductor [11]. Briefly, for each sample, the HDF5 file generated by Cell Ranger was imported into R to create a SingleCellExperiment object. A combination of median absolute deviation (MAD), as implemented by the “isOutlier” function in the scuttle R package (v1.4.0) and exact thresholds were used to identify and subsequently remove low-quality cells before data integration.

Data integration, visualisation and cell clustering

The log-normalised expression values of the combined data were re-computed using the "multiBatchNorm" function from the bachelor R package (v1.10.0). The per-gene variance of the log-expression profile was modelled using the "modelGeneVarByPoisson" function from the scran R package (v1.22.1), and the top 5000 highly variable genes were selected. The mutual nearest neighbours (MNN) approach implemented by the "fastMNN" function from the bachelor R package was used to perform batch correction.

The first 50 dimensions of the MNN low-dimensional corrected coordinates for all cells were used as input to produce the t-stochastic neighbour embedding (t-SNE) projection and uniform manifold approximation and projection (UMAP) using the "runTSNE" and "runUMAP" functions from the scater R package (v1.22.0) respectively.

Putative cell clusters were identified using the Leiden algorithm from the igraph R package (v1.3.0).

Marker genes and differential expression analysis

Cluster-specific markers were identified using the "findMarkers" function from the scran R package, which performs pairwise t-tests between clusters. Differential expression analysis between treatment and control (IgG) was performed on pseudo-bulk samples using the quasi-likelihood pipeline from the edgeR R package (v3.36.0). Genes with a false discovery rate (FDR) below 5% were considered differentially expressed.

Pathway analysis

Pathway enrichment analysis of differentially expressed genes was performed using the R package enrichR (v3.0). Pathway results were ranked by the combined scores (calculated as log(P-value) multiplied by z-score), and pathways with an adjusted P-value < 0.05 were considered significant.

Further gene set enrichment analysis GSEA was done using Metascape web tool [12] and plotted as $-\log_{10}P$.

Subclustering and further analysis

Cells were divided into functional cell type groups and further subclustered using the Louvain method for community detection [13].

Trajectory inference was made using the Slingshot R package [14], and the association of our PARP14i signature with survival in immune checkpoint blockade therapy(ICBT) cohorts, as well as a comparison of high and low-expressed genes in specific clusters, was assessed using Tumour Immune Dysfunction and Exclusion (TIDE) web tool [15]. Sample RL1i projection on UMAP was done using ProjecTILs R package [16].

Data Availability

Single-cell RNAseq data have been deposited in the ArrayExpress database at EMBL-EBI under accession number E-MTAB-14471. Bulk RNA sequencing was performed as previously described [5], with data available from the ArrayExpress database under accession numbers E-MTAB-12195 and E-MTAB-12872.

Results

A genetic signature reflecting the modulating effect of PARP14i on chronic IFNγ stimulation predicts response to α-PD-1 in clinical cohorts

We and others have previously shown the role of PARP14 in modulating type II interferon signalling [5,8,17]. Following chronic stimulation of several mouse and human cancer cell lines with Interferon-γ (IFNγ) and then subsequent treatment for 48 hours with a PARP14 inhibitor (PARP14i), PARP14 PROTAC or DMSO (drug solvent control), we assessed differences in gene expression by bulk RNA sequencing (RNAseq). Comparison of the top 50 differentially expressed genes within each cell model revealed a shared expression pattern, which we narrowed down to a PARP14i signature consisting of 30 genes **(FIGURE 1A, SUPPLEMENTARY FIGURE 1 and SUPPLEMENTARY TABLES)**. Pathway enrichment analysis performed by Metascape [12] and ARCHS4 [18] revealed that among this signature were genes strongly correlated with response to IFNγ signalling, with a focus on STAT/IRF regulation **(FIGURE 1B and SUPPLEMENTARY FIGURE 2).** However, we found this signature is distinct from the genes contained with the IFNγ signalling GO term, with less than half of the PARP14i signature displaying overlap. We then investigated whether this PARP14i signature could predict response to α-PD-1 therapy by employing Tumour Immune Dysfunction and Exclusion (TIDE) analysis [15]. High expression of genes within this signature was associated with substantial improvement in overall patient survival across several clinical cohorts

261 receiving immune checkpoint blockade therapy [19–21] **(FIGURE 1C)**, underscoring the
262 prognostic value of this signature and supporting the potential therapeutic benefit of
263 PARP14 inhibition.
264
265 Furthermore, we performed RNAseq analysis on subcutaneous tumours comprising
266 YUMM2.1 cells dissected from mice treated with either IgG or α-PD-1, dividing the latter
267 into those either relapsing or responding to the treatment. Although the PARP14i signature
268 was upregulated in α-PD-1-treated samples, it did not distinguish between treatment
269 response and relapse (**FIGURE 1D**). For further comparison, we also analysed IgG-treated
270 tumours arising from YUMM2.1 cells pre-treated *ex vivo* with chronic IFNγ before
271 implantation and found that the PARP14i signature was significantly downregulated,
272 indicating a Tumour Microenvironment (TME) which is T cell cold and inherently resistant to
273 α-PD-1.
274

275 **Analysis of changes to the cellular composition of YUMM2.1 tumours relapsing following**
276 **α-PD-1 therapy driven by subsequent PARP14 inhibitor treatment**

277 To investigate further the ability of PARP14i to improve α-PD-1 response, we turned to our
278 previously described mouse model of acquired resistance [5]: YUMM2.1 cells were
279 implanted subcutaneously, and upon tumours reaching ~80mm^3 in volume, two doses of α-
280 PD-1 antibodies were given three days apart **(FIGURE 2A and SUPPLEMENTARY FIGURE 3A)**.
281 Tumour volumes were routinely recorded and at ~100-150mm^3, animals were randomly
282 allocated into the following re-treatment groups: IgG2a (n=4); α-PD-1 (n=3); PARP14i alone
283 (n=3); and a combination of α-PD-1 + PARP14i (n=4). Animals were sacrificed following seven

284 days of re-treatment, and tumours were subsequently processed for single-cell RNA
285 sequencing (scRNAseq). Following tumour dissociation and enrichment for $CD45^+$ cells, 5%
286 from the $CD45^-$ cell fraction was added to ensure tumour cell representation in our analyses.
287 Cells were fixed and frozen until all tumour samples were collected; then, samples were
288 barcoded, multiplexed, and libraries prepared and sequenced.
289
290 In total, fourteen samples of tumour immune cells were sequenced. Initial analysis of
291 sequencing data identified one of the IgG samples (RL11i) to be anomalous, which upon
292 further review of its corresponding tumour growth curve was attributed to it being, in
293 reality, a non-responder to the initial α-PD-1 treatment, and therefore, it was excluded from
294 subsequent analyses (**SUPPLEMENTARY FIGURE 3A-C)**. Leiden unsupervised clustering
295 across the remaining thirteen treated samples identified twenty-eight clusters based upon
296 gene expression patterns, with a diverse range of cell types represented across samples and
297 treatment groups **(FIGURE 2B and SUPPLEMENTARY FIGURES 3C and D)**. The following cell
298 types were identified: Monocytes (Clusters 1-5); Macrophages (6-8); B cells (9-10); Plasma
299 cells (11); Natural Killer (NK) cells (12); T cells (13-17); Dendritic cells (18-21); Granulocytes
300 (22-25); Cancer-Associated Fibroblasts (26); and Tumour cells (27-28). To characterise the
301 individual clusters within these groups, we manually validated cell type identity by
302 comparing the expression of known markers across clusters **(SUPPLEMENTARY TABLES)**.
303
304 Macrophages, Monocytes and T cells were the most abundant leukocyte populations across
305 all treatment groups, with distinct subpopulations displaying treatment-specific enrichment
306 **(SUPPLEMENTARY FIGURE 3E)**. Notably, T cells were particularly abundant in combination-
307 treated samples, with increased prevalence of clusters 14 and 16 and depletion of cluster 13,

308 which was highly enriched in IgG-treated samples **(FIGURE 2C)**. Similarly, analysis by cell
309 density plots revealed a shift from cluster 7 in macrophages, prominent in α-PD-1 -treated
310 samples, towards cluster 6 in the PARP14i and combination treatments **(FIGURE 2D)**.
311 Furthermore, we observed IgG-specific enrichment and depletion of B cells and monocytes,
312 respectively. Similarly, across our treatment cohort, few neutrophils and eosinophils were
313 identified, and these could not be well separated, yet we found the sequenced tumour
314 sample, which did not respond to α-PD-1 to be highly enriched in neutrophils
315 (**SUPPLEMENTARY FIGURE 3B**), consistent with a documented role of neutrophils in
316 promoting rapid tumour growth [22].
317

318 **PARP14 inhibitor treatment in combination with α-PD-1 therapy drives activated cytotoxic**
319 **T cells and limits their transition to dysfunctional states**

320 To further characterise specific T cell identities and assess their functionality, we conducted
321 subclustering of clusters 12-17 from the initial clustering **(FIGURE 3A).** By combining NK and
322 T cells for further subclustering, we can be confident that our new T cell clusters are free
323 from any contaminating readouts due to the presence of NK T cells. This subclustering can
324 be split broadly into NK cells (1-5) and T cells (6-19), with key subpopulations including naïve
325 T cells (7 and 19), regulatory T cells (Tregs) (10 and 11), and cytotoxic T cells (13-18).
326 Comparing the proportions of each T cell subcluster revealed treatment-specific changes in
327 cellular identity and function **(FIGURE 3B).** Cell density mapping **(FIGURE 3C)** highlighted a
328 treatment-dependent decrease in naïve T cells (subcluster 7), which were highly abundant in
329 IgG-treated samples, suggesting their transition into differentiated or activated states. These
330 naïve T cells also exhibited increased Sell expression compared to other T cell subclusters,

331 indicative of early activation **(SUPPLEMENTARY FIGURE 4A)**. This suggests that IgG-treated
332 tumours suffer from inefficient antigen presentation due to dysfunctional priming by
333 Antigen-Presenting Cells (APCs), which fail to deliver essential differentiation signals to naïve
334 T cells.
335
336 Corroborating our hypothesis that the reduction in naïve T cells is due to their differentiation
337 into more active T cell states, we identified a significant enrichment amongst all cytotoxic T
338 cell clusters in the combination treatment group. Detailed gene expression analysis revealed
339 that T cell subclusters 13-16 exhibit distinct characteristics associated with T cell exhaustion,
340 quiescence, hyperactivation and T cell response, respectively (**FIGURE 3D & E)**. In the
341 context of anti-tumour activity, these states are closely interconnected in driving the T cell
342 effector response. T cell exhaustion is associated with poor clinical outcomes due to loss of T
343 cell functionality, which fails to control tumour progression [23]. Our slingshot trajectory
344 analysis (**FIGURE 3F)** indicates that by entering a state of dormancy, quiescent cytotoxic T
345 cells (subcluster 14) avoid a state of hyperactivity (subcluster 15), also evading exhaustion
346 (subcluster 13) in the presence of chronic antigen stimulation. Herein, these quiescent cells
347 can either undergo reactivation that avoids terminal exhaustion (subcluster 16) or persist as
348 a reservoir of memory T cells with retained effector function, poised for re-activation.
349
350 TIDE analysis was performed using gene expression signatures arising from each T cell
351 subcluster from subclusters 13-16, revealing that high expression of the gene signature for
352 subcluster 16 (reactivated T cells) was associated with significantly improved survival of
353 patients receiving immune checkpoint blockade therapy (**FIGURE 3G**). Furthermore, we
354 observed this was also true, albeit to a lesser degree, for the gene signatures arising from

355 subclusters 14 (quiescent T cells) and 15 (hyperactive T cells). On the other hand, the gene
356 signature of T cell subcluster 13 (exhausted T cells) did not associate with positive patient
357 outcomes, possibly due to heterogeneity in T cell exhaustion phenotypes within this cluster.
358 This suggests that cells within subclusters 14–16 are critical in mounting an effective anti-
359 tumour response through mechanisms which sustain effector function without succumbing
360 to terminal exhaustion.
361
362 We next employed Single-Cell rEgulatory Network Inference and Clustering (SCENIC) [24] to
363 highlight transcriptional regulatory systems that are most pertinent to the functional and
364 prognostic characteristics of these T cell populations and revealed distinct regulatory
365 patterns across the T cell subclusters, highlighting the differential activity of several key
366 transcription factors (**FIGURE 3H and SUPPLEMENTARY FIGURE 4D)**. *Jdp2*, an AP-1 repressor,
367 exhibited differential regulon activity across the T cell subclusters, being elevated in
368 subcluster 13 compared to subclusters 14-16. Higher *Jdp2* expression contributes to
369 impaired cellular functionality by T cell exhaustion and anergy [25,26]. Therefore, lower
370 activity of the *Jdp2* regulon in subclusters 14 and 15 is consistent with a more functional and
371 active T cell state and, considering the enrichment of these subclusters with Combination
372 treatment supports the notion that decreased *Jdp2* activity facilitates better immune
373 responses. Furthermore, elevated activity of the *Mxd1* regulon in subcluster 13 suggests
374 this, too, has a crucial role in maintaining the exhausted state characteristic of this
375 subcluster by repressing cellular growth, contributing to its adverse clinical outcomes [27].
376 Antagonistic roles of *Mxd1* and *Myc* have been widely reported [28]. It is consistent,
377 therefore, that the *Myc* regulon was notably active in T cell subclusters 14 and 15, which are
378 linked to better prognoses and effective anti-tumour responses. Elevated *Myc* activity in

these clusters indicates a role that supports T cell activation and functionality via increased metabolic and proliferative activities that promote more robust and favourable immune responses. Taken together, these relationships aid our understanding of ways in which transcriptional networks influence T cell states and responses within the TME.

The findings from our cytotoxic T cell subclustering and gene expression analyses are further supported by bulk RNAseq data obtained from the YUMM2.1 subcutaneous tumours described earlier. Focussing mostly on α-PD-1 relapsing versus responding tumours, these analyses provide a broader context for understanding the immune dynamics at play in the TME. In agreement with other studies, IFNγ pre-treatment led to the development of an 'immune desert' in the TME, characterised by a marked reduction in immune cell infiltration. In contrast, IgG-treated naïve tumours exhibited higher levels of T cell activation and exhaustion, reflecting an active yet ultimately ineffective immune response **(SUPPLEMENTARY FIGURE 4B)**. Interestingly, tumours relapsing on α-PD-1 therapy displayed even higher levels of T cell activation and exhaustion than those treated with IgG alone, which suggests that despite the robust initial immune response, these tumours managed to evade sustained immune control. Conversely, α-PD-1 responding tumours displayed lower levels of exhaustion and elevated markers of T cell hyperactivation, consistent with a robust anti-tumour response. These bulk RNAseq findings align with our scRNAseq data, indicating that Combination therapy may successfully replicate the T-cell activation patterns seen in α-PD-1 responders. As the literature suggests activities which both elicit pro-inflammatory responses and mediate tumour progression for hyperactivated T cells [29,30], our TIDE analysis suggests the correlation with positive responses to α-PD-1 may be transient and

402 insufficient for long-term tumour control, emphasising the need for more durable
403 therapeutic interventions.
404
405 To further explore the immune landscape shaped by Combination therapy, we performed
406 flow cytometry analysis of α-PD-1 relapsing tumours treated with either α-PD-1 or
407 Combination therapy. Building on our observations of T cell dynamics, this revealed shifts in
408 T cell populations following Combination treatment compared to α-PD-1 treated tumours
409 **(FIGURE 3I)**. Specifically, Combination treatment reduced T cell cytotoxicity **(FIGURE 3J)** and
410 was accompanied by nuanced changes in the expression of immune checkpoint markers. We
411 observed a decrease in LAG-3 positivity in PD-1^{+} CD8^{+} T cells, associated with reduced T cell
412 exhaustion and an enhancement of immune response. However, this was counterbalanced
413 by increased TIM-3 expression, another marker linked to T-cell dysfunction and exhaustion
414 **(FIGURE 3K)** [31,32]. Further examination of PD-1^{+}CTLA-4^{+} CD8^{+} T cells showed that
415 Combination treatment had limited impact on reversing terminal exhaustion, likely due to
416 the combined inhibitory effects of multiple markers **(FIGURE 3L)**. Further analysis, focused
417 on the PD-1^{+}CTLA-4^{-} population, suggested that LAG-3 and CTLA-4 are co-dependent in this
418 context **(FIGURE 3M)**. This suggests that targeting each alone as a further intervention may
419 prove ineffective. Together, these findings highlight the complexity and heterogeneity of T
420 cell states in the TME that influence therapeutic efficacy.
421

PARP14 inhibitor treatment increases M1 macrophage polarisation to generate a memory-like state

Given the previous demonstration that PARP14i can suppress M2 macrophage differentiation and mimic α-PD-1 treatment in renal tumour explants [7], we expanded our investigation to the macrophage populations in the TME. By further subclustering clusters 1-8 from the initial analysis, we created a new MonoMac UMAP representation detailing a clear division of these subclusters into either those which exhibited characteristics of M1 macrophages (Left) or M2 macrophages (Right) (**FIGURE 4A** and **SUPPLEMENTARY TABLES)**.

Analysis of cell type proportions within this subclustering revealed treatment-specific changes. Combination treatment notably shifted macrophage polarisation from M2 towards M1 (**FIGURE 4B**). Further inspection of gene enrichment analysis of DEGs, applied alongside cell density mapping, allowed us to robustly identify subclusters most affected by treatment **(FIGURE 4C)**. This demonstrated that subcluster 10— the most abundant cluster in the IgG-treated samples— is effectively depleted by Combination treatment **(FIGURE 4D)**. This subcluster consists primarily of tumour-associated macrophages (TAMs), which are known to facilitate tumour progression and metastasis, and as such, their reduction by Combination treatment disrupts pro-tumoural mechanisms.

These anti-tumoural effects are further supported by the expansion of specific macrophage clusters. The increase in M1 macrophages (subcluster 2) signifies an enhanced pro-inflammatory response through Th1 pathways that bolsters anti-tumour immunity. Similarly, the increased abundance of a transitory M1/M2 macrophage state (subcluster 4) further illustrates the dynamic changes in macrophage populations, highlighting cellular plasticity

446 modulated by Combination treatment to influence the balance between inflammatory and
447 immunoregulatory activities. Concurrently, macrophage subcluster 8, representing M2a
448 macrophages, exhibits an expression pattern that supports tissue repair and dampening
449 excessive inflammation in the tumour.
450
451 The overall increase in M1 macrophages following Combination treatment is linked to
452 reduced *Tgm2*, *Vegfa* and *Cebpb* expression, key drivers of M2 macrophage polarisation
453 **(FIGURE 4E)** [33]. Their expression patterns observed in subclusters 8 and 10 align with the
454 depletion of M2-related clusters and the relative enrichment of M2a macrophages induced
455 by Combination treatment, reinforcing the transition towards a more hostile tumour
456 environment. Additionally, PARP14i treatment results in a marked downregulation of *Nfatc1*,
457 *Nfatc3* and *Smad4* across subclusters (**FIGURE 4E)**, reducing *Tgfb1* signalling in M2
458 macrophages, as evidenced by lower *Sox2* and *Sox4* expression [34]. This corresponds with
459 diminished pro-inflammatory gene expression, while the decreased expression of *Stat3*,
460 *Stat6* and *Jun* in subclusters 2 and 4 correlates with reduced transcriptional activity and
461 cellular activation. These changes suggest subclusters 2 and 4 are similar to T cell subcluster
462 14 in that they may represent memory-like cells with the potential for re-activation [35].
463
464 Crucially, the interaction between immune cell subsets largely defines their activities.
465 Contact between PILRA and CD8α was previously shown to maintain cytotoxic T cells in a
466 quiescent state [36]. Therefore, elevated *Pilra* expression in M1-like subclusters likely serves
467 as a barrier to prevent premature re-activation (**FIGURE 4E)**. Given that *Pilra* correlates
468 positively with tumour immune infiltration and prognosis [37], its elevated expression in

subclusters enriched by Combination treatment supports the establishment of quiescent T cells.

To further explore the molecular underpinnings of macrophage polarisation, we applied SCENIC analysis to evaluate transcriptional regulatory programs within these subclusters **(FIGURE 4F)**. Here, we identified regulons which effectively delineated M1 (*Runx3* and *Cux1*) and M2 (*Irf4*) macrophages. Additionally, six regulons associated with M2 macrophages (*Nfia, Nr1d1, Klf2, Klf3, Etv1, Dbp*) were most strongly associated with subcluster 10. In the context of Combination treatment, the depletion of subcluster 10 resulted in a significant reduction in the activity of these regulons. However, this reduction may be offset by the enrichment of subcluster 8, indicative of a directional shift in this treatment towards an M1-like phenotype. These findings suggest that the overall balance between M1 and M2 macrophages is shifting towards a pro-inflammatory, anti-tumour state in Combination treatment. Notably, subclusters 2 and 4, despite their relatively low regulon activity beyond the M1-defining features, may represent more memory-like macrophage states.

Combined α-PD-1 and PARP14 inhibitor treatment provokes dynamic adaptive resistance strategies in tumour cells

To further understand the impact of PARP14 inhibition on the TME, we further subclustered tumour cells and Cancer-Associated Fibroblasts (CAFs)— covering clusters 26-28— into six distinct subclusters **(FIGURE 5A)**, each exhibiting different characteristics which reflect their roles in tumour growth, progression and adaptive responses to therapy. For instance, compared with IgG, α-PD-1 treatment alone effectively doubled the size of tumour

492 subcluster 3, comprising stem-like cells (**FIGURE 5B and C**). This tumour subcluster was
493 found by slingshot trajectory analysis [14] to be the origin of tumour cell types associated
494 with immunomodulation and immune evasion— subclusters 4 and 5— (**FIGURE 5D**). Their
495 stem-like qualities are particularly evident when surveying Gene Set Enrichment Analysis
496 (GSEA) outputs for this tumour subcluster (**FIGURE 5E**). Therefore, suppression of this
497 subcluster by combination treatment indicates how a more potent treatment response is
498 associated with reducing the stemness of tumour cells, thereby limiting self-renewal
499 capacity and disrupting cell survival pathways.
500
501 In contrast, tumour subclusters 1, 2 and 4 were enriched by Combination treatment.
502 Tumour-subcluster 2, the most prominent of these and notable for its highly invasive and
503 adhesive cells, plays a crucial role in tumour metastasis through extracellular matrix
504 remodelling. Its enrichment demonstrates, we infer, an adaptive response to evade immune
505 attack under intense therapeutic pressure, as evidenced by increased activation of
506 biosynthetic pathways (**FIGURE 5E**). Similarly, the angiogenic and epithelial-mesenchymal
507 transition (EMT) phenotypes shared by cells within tumour subcluster 1 reflect their
508 migratory and metastatic capacity. As shown by pathway enrichment analyses, DEGs in this
509 subcluster support tumour growth, vascularisation and metastasis whilst also dampening
510 immune responses (**FIGURE 5E**). The increased activation of metabolic pathways in tumour
511 subcluster 4 suggests that the Combination treatment enhances proliferative potential and
512 cellular turnover, which could inadvertently support aggressive tumour growth. This
513 behaviour is characteristic of tumours with high resistance to therapy, which sustain growth
514 and repair mechanisms despite treatment. Furthermore, GSEA reveals these strategies likely
515 involve elevated angiogenesis, cell expansion and interference with immune cell recognition

516 machinery (**FIGURE 5E**). Therefore, while treatment suppresses key tumour-promoting
517 pathways such as stemness, it can also select tumour adaptations which permit immune
518 escape.
519
520 Across these tumour subclusters, we evaluated the top 200 upregulated genes and extracted
521 those uniquely upregulated in each subcluster. We then visualised the expression of each
522 subcluster's gene list in our bulk RNAseq data for the previously described YUMM2.1
523 subcutaneous tumours. Here, we found that the gene lists for subclusters 1, 2 and 5 were
524 more strongly associated with tumours relapsing on α-PD-1 treatment, whereas genes from
525 subclusters 3 and 4 correlated with tumours that responded to α-PD-1 (**SUPPLEMENTARY**
526 **FIGURE 6A)**. Furthermore, when evaluating these unique gene lists using TIDE, these were
527 largely in agreement with our identification of relapse or response outcomes with subcluster
528 4, which responds to α-PD-1 treatment, resulting in improved patient survival
529 (**SUPPLEMENTARY FIGURE 6B).** Similarly, signatures for subclusters relapsing on α-PD-1
530 therapy were associated with worse clinical outcome. However, concerning genes uniquely
531 upregulated in subcluster 3, the inability of this signature to predict clinical response
532 suggests that this subcluster of cells can follow different paths under selective pressure,
533 transitioning into states that are either susceptible to immune attack or capable of evading
534 immune defences. It is this balance between vulnerability and evasion that ultimately
535 determines the overall treatment outcome.
536
537 When next we queried the previously identified PARP14i signature within the subclusters,
538 we observed treatment- and subcluster-specific regulation of many genes within this
539 signature **(FIGURE 5F)**. In tumour subcluster 1, Combination treatment upregulated many of

these genes, indicating elevated interferon signalling, while in subcluster 4, these are downregulated, reflecting reduced metabolic and proliferative activity. Similarly, most genes within this signature are enriched in tumour subcluster three following α-PD-1 treatment alone, yet Combination treatment limits PD-1-driven upregulation for many of these, potentially to prevent chronic stimulation. In subcluster 2, responses were more gene-specific, with both PARP14i and combination treatments reducing *Ifit3* and elevating *Gbp7* expression, suggesting a shift towards increased Type II interferon signalling.

Discussion

The therapeutics currently used for melanoma, particularly immune checkpoint inhibitors (ICIs) such as α-PD-1, have made a significant impact but still face considerable challenges. One of the most persistent problems is tumour resistance. Although combination therapies and targeted agents have been investigated, they have only been partially successful in overcoming resistance mechanisms [38,39]. This ongoing challenge underscores the necessity for novel interventions that can enhance treatment efficacy by more effectively addressing resistance. Our previous research demonstrated that PARP14, a crucial regulator of immune responses and chromatin dynamics, can modulate the TME and that its inhibition boosts the activity of infiltrating T cells [5]. However, these findings were limited by an incomplete understanding of how PARP14 impacts immune cell dynamics. In this study, we

address these gaps by investigating the effects of combining PARP14 inhibition with α-PD-1 therapy on the tumour immune infiltrate at the onset of α-PD-1 resistance.

A central challenge in overcoming resistance is T cell exhaustion, where prolonged antigen exposure causes T cells to lose their functional capacity [40,41]. This state is characterised by the upregulation of inhibitory receptors and a corresponding decline in cytokine production and cytotoxic activity. Rather than inducing terminal exhaustion, we found that the combination therapy triggered a unique strategy to evade exhaustion characterised by hyperactivated T cells entering a state of quiescence. Elevated expression of genes associated with T cell hyperactivation contribute to a pro-inflammatory environment; however, this may exacerbate tumour progression if inflammation is excessive [29] rather than effectively controlling it [30]. This implies that to maintain a productive anti-tumour response, T cells must employ an exit strategy, such as entering quiescence, which prevents terminal T-cell exhaustion but also limits hyperactivation. Unlike classical exhaustion, where T cells lose all activation markers, the quiescent T cells in our study retained a gene expression pattern associated with longevity (eg. *Bcl2*, *Il-6*) compared with exhausted states. This reservoir could potentially be leveraged by integrating further therapeutics designed to reactivate these T cells.

The role of Pilra interactions as a driver of T cell quiescence presents a potential axis for such an intervention. Intriguingly, the Pilra ligand CD8α was highly expressed in T cell subcluster 14 and even more so in subcluster 16, suggesting that overcoming PILRA inhibition may be necessary to exit the quiescent state. Predictions of better patient prognosis in tumours

highly expressing *Pilra* support a strategy to evade T cell exhaustion by entering quiescence [37]. Although the use of a monoclonal antibody therapeutic specific to PILRA has not yet been explored in cancer treatment, preclinical models have shown promising results in the context of autoinflammatory diseases [42,43]. Targeting the PILRA-CD8α axis could thus reinvigorate quiescent T cells to generate T cell states with a more active anti-tumour response (e.g. T cell subcluster 16).

Moreover, PARP14 inhibition reduced immunosuppressive signals, fostering a more pro-inflammatory environment that enhanced T cell activation and function. This effect is particularly noteworthy as a potential means of counteracting the T cell dysfunction often associated with markers of ICI resistance, such as chronic IFNγ exposure. We observed that inhibiting PARP14 induced a significant shift from an immunosuppressive TME, typically linked with M2 macrophages, to a more inflammatory state characterised by increased polarisation towards an M1 phenotype, in keeping with previous findings [7,8]. M2 macrophages are typically exploited by tumours for their roles in tissue repair and immunosuppression to create a microenvironment that facilitates tumour progression [44,45]. Conversely, M1 macrophages, known for their production of pro-inflammatory cytokines such as TNF-α, IL-1β, and IL-6, are instrumental in orchestrating and sustaining effective anti-tumour immune responses [46,47]. Therefore, by generating a more immunostimulatory and anti-tumour environment, PARP14 inhibition can be utilised to overcome immune evasion strategies employed by tumours [48]. In addition to their direct anti-tumour effects, enrichment of M1 macrophages by PARP14i also promotes the production of cytokines and chemokines that recruit and activate T cells [49,50].

Consequently, M1 macrophages can enhance the effectiveness of PD-1 blockade therapy by increasing the infiltration and activation of cytotoxic T cells within the tumour.

The activity of PARP14 in chromatin remodelling and gene expression regulation impacts key immune pathways through its interaction with *STAT1* [8], *STAT3* [51] and *STAT6* [52]. Following cytokine stimulation, PARP14 modulates the accessibility of these promoter regions through its interaction with HDACs, facilitating transcription factor recruitment [52]. Recent studies highlight the critical role of epigenetic regulation for macrophage polarisation, which determines their functional state, whilst quiescent T cells actively manage their epigenetic landscape to remain poised for rapid reactivation while preserving their long-term functionality [53]. In the context of combination therapy, our PARP14i intervention occurs following this stimulation. Thus, we speculate that PARP14 inhibition prevents the re-recruitment of HDACs to the promoter regions, leading to a "dormant" memory state in T cells and macrophages while retaining essential readiness for reactivation of immune cell responsiveness. This illustrates the influence of PARP14 upon the regulation of chromatin dynamics, with the capacity to alter immune cell responsiveness and functionality in the TME, emphasising the therapeutic potential of modulating such pathways.

Despite the positive effects of our novel therapeutic combination, our study also underscores the concept of dynamic adaptive resistance, wherein tumour cells rapidly evolve in response to therapeutic pressure. Although the combination of α-PD-1 and PARP14 inhibition initially enhances immune responses, tumour cells can engage alternative pathways and modulate immune checkpoints, allowing them to evade immunotherapy and

634 persist despite intensified immune pressure. This observation highlights the remarkable
635 adaptability within the TME and aligns with findings from other studies that have reported
636 similar resistance phenomena in response to targeted therapies [54,55].
637
638 Our investigation revealed a robust PARP14 inhibition (PARP14i) gene signature that is
639 strongly associated with IFNγ signalling and STAT/IRF pathway regulation. While this
640 signature was upregulated in α-PD-1-treated samples, it did not differentiate between
641 treatment response and relapse in our preclinical model. Nonetheless, the high expression
642 of these genes correlates with improved patient survival, supporting the potential of
643 PARP14i to enhance the efficacy of PD-1 blockade. This suggests that, despite an initial
644 sensitivity to PD-1 blockade resulting in total tumour eradication, residual YUMM2.1 cells
645 that have developed resistance to α-PD-1 adapt rapidly to further therapeutic
646 interventions—possibly by acquiring more stem-like characteristics over time, which
647 subsequently enable tumour growth even in the presence of a re-established immune
648 response. Consequently, the subcluster-specific effects of combination therapy in tumour
649 cells indicate that, although combination therapy enhances T cell activation and
650 inflammation, alterations in the expression of the PARP14i gene signature combined with
651 mounting immune pressure when combined with α-PD-1 treatment may simultaneously
652 facilitate the development of resistance mechanisms that allow tumour persistence. Notably,
653 the upregulation of *Stat1*, *Atf3*, *Irf1*, and *Cd274* in the EMT angiogenic tumour cells within
654 tumour subcluster 1 suggests that combination treatment may inadvertently enhance EMT-
655 associated properties, thereby promoting more invasive and immune-evasive tumour cells
656 [56]. Conversely, given the role of IFNγ in regulating many genes within this signature, the
657 downregulation of these genes in tumour cells of tumour subcluster 4 suggests reduced

intrinsic IFN signalling, which could potentially increase their susceptibility to immune-mediated destruction despite their high proliferative activity [57]. This dual effect underscores the complexity of targeting regulatory pathways involved in tumour immunity and illustrates the delicate balance between tumour cell expansion and immune attack.

The observed adaptive resistance underscores the necessity for a multifaceted approach to cancer treatment. As adaptive resistance mechanisms can evolve rapidly, our findings indicate that the initial benefits of combining α-PD-1 therapy with PARP14 inhibition may be counteracted by subsequent resistance. Therefore, future research must focus on developing multi-modal strategies that integrate immune checkpoint inhibitors with agents that both target the tumour and enhance a pro-inflammatory immune infiltrate within the TME, potentially leading to more durable patient responses. Moreover, our identification of a PARP14i gene signature offers therapeutic promise, particularly for patients in whom expression of these genes is low. By utilising this gene signature as a biomarker, clinicians can more accurately identify patients who are likely to benefit from PARP14 inhibition, facilitating a more personalised and targeted treatment approach. This not only optimises treatment efficacy but also helps avoid unnecessary interventions in patients who are less likely to respond. Additionally, there is potential to further refine this approach by identifying supplementary interventions that could be combined with PARP14 inhibition. The precise mechanism that unlocks T cell potential in the Combination treatment is unclear, requiring further investigation to determine whether combination treatment prevents tumour cells from down-regulating their antigens through dedifferentiation or reverses an inhibitory mechanism impairing T cell-APC interactions. If future studies can identify agents that either target complementary pathways or prevent the adaptive resistance observed in

tumour cells, it may be possible to develop more robust combination therapies. Interventions that synergise with PARP14i and α-PD-1 could potentially overcome even the most resilient tumour populations, ultimately providing a more durable and comprehensive therapeutic response.

Declarations

Acknowledgements

This study was funded by a research sponsorship agreement between Ribon Therapeutics and The University of Manchester, grant 821034 from the Melanoma Research Alliance (MRA), grant 22-0091 from Worldwide Cancer Research (WCR), and an award from the Skin Cancer Research Fund (SCaRF). C.W.W. was funded by a scholarship from the Hong Kong Scholarship for Excellence Scheme (HKSES). We thank Dr Gareth Howell and The University

of Manchester Flow Cytometry Core Facility for facilitating flow cytometry analysis, Dr Andy Hayes and Claire Morrisroe in the Genomic Technologies Core Facility for assistance with single-cell RNA sequencing, Dr Leo Zeef and the Bioinformatics Core facility for their help with bioinformatic analysis, and members of the Biological Services Facility at The University of Manchester for help with animal work. FIGURE 2A and Graphical Abstract were created using BioRender.

Author Contributions Statement

A.H. conceived the study. R.L., K.N.S., and C.W.W. performed experiments. I.L. and R.L. analysed the scRNAseq data. K.N.S. analysed the flow cytometry and bulk RNAseq data. D.T.I., M.N., and A.H. contributed to experimental design and data analysis. R.L., K.N.S., and A.H. drafted the original version of this manuscript, with all authors reviewing subsequent drafts. A.H. obtained funding for the study.

Competing Interests Statement

The authors declare the following competing interests:

D.T.I. and M.N. were employees and shareholders of Ribon Therapeutics at the time of data collection. A.H. received research sponsorship from Ribon Therapeutics. All other authors declare no competing interests.

References

[1] Ribas A, Hamid O, Daud A, Hodi FS, Wolchok JD, Kefford R, et al. Association of Pembrolizumab With Tumor Response and Survival Among Patients With Advanced Melanoma. JAMA 2016;315:1600. https://doi.org/10.1001/jama.2016.4059.

[2] Lim J, Kang I, La J, Ku KB, Kang BH, Kim Y, et al. Harnessing type I interferon-mediated immunity to target malignant brain tumors. Front Immunol 2023;14:1203929. https://doi.org/10.3389/fimmu.2023.1203929.

[3] Qiu J, Xu B, Ye D, Ren D, Wang S, Benci JL, et al. Cancer cells resistant to immune checkpoint blockade acquire interferon-associated epigenetic memory to sustain T cell dysfunction. Nat Cancer 2023. https://doi.org/10.1038/s43018-022-00490-y.

[4] Benci JL, Johnson LR, Choa R, Xu Y, Qiu J, Zhou Z, et al. Opposing Functions of Interferon Coordinate Adaptive and Innate Immune Responses to Cancer

Immune Checkpoint Blockade. Cell 2019;178:933-948.e14. https://doi.org/10.1016/j.cell.2019.07.019.

[5] Wong CW, Evangelou C, Sefton KN, Leshem R, Zhang W, Gopalan V, et al. PARP14 inhibition restores PD-1 immune checkpoint inhibitor response following IFNγ-driven acquired resistance in preclinical cancer models. Nat Commun 2023;14:5983. https://doi.org/10.1038/s41467-023-41737-1.

[6] Meeth K, Wang JX, Micevic G, Damsky W, Bosenberg MW. The YUMM lines: a series of congenic mouse melanoma cell lines with defined genetic alterations. Pigment Cell Melanoma Res 2016;29:590–7. https://doi.org/10.1111/pcmr.12498.

[7] Schenkel LB, Molina JR, Swinger KK, Abo R, Blackwell DJ, Lu AZ, et al. A potent and selective PARP14 inhibitor decreases protumor macrophage gene expression and elicits inflammatory responses in tumor explants. Cell Chem Biol 2021;28:1158-1168.e13. https://doi.org/10.1016/j.chembiol.2021.02.010.

[8] Iwata H, Goettsch C, Sharma A, Ricchiuto P, Goh WWB, Halu A, et al. PARP9 and PARP14 cross-regulate macrophage activation via STAT1 ADP-ribosylation. Nat Commun 2016;7:12849. https://doi.org/10.1038/ncomms12849.

[9] Caprara G, Prosperini E, Piccolo V, Sigismondo G, Melacarne A, Cuomo A, et al. PARP14 Controls the Nuclear Accumulation of a Subset of Type I IFN–Inducible Proteins. J Immunol 2018;200:2439–54. https://doi.org/10.4049/jimmunol.1701117.

[10] Wigle TJ, Ren Y, Molina JR, Blackwell DJ, Schenkel LB, Swinger KK, et al. Targeted Degradation of PARP14 Using a Heterobifunctional Small Molecule. ChemBioChem 2021;22:2107–10. https://doi.org/10.1002/cbic.202100047.

[11] Amezquita RA, Lun ATL, Becht E, Carey VJ, Carpp LN, Geistlinger L, et al. Orchestrating single-cell analysis with Bioconductor. Nat Methods 2020;17:137–45. https://doi.org/10.1038/s41592-019-0654-x.

[12] Zhou Y, Zhou B, Pache L, Chang M, Khodabakhshi AH, Tanaseichuk O, et al. Metascape provides a biologist-oriented resource for the analysis of systems-level datasets. Nat Commun 2019;10:1523. https://doi.org/10.1038/s41467-019-09234-6.

[13] Blondel VD, Guillaume J-L, Lambiotte R, Lefebvre E. Fast unfolding of communities in large networks. J Stat Mech Theory Exp 2008;2008:P10008. https://doi.org/10.1088/1742-5468/2008/10/P10008.

[14] Street K, Risso D, Fletcher RB, Das D, Ngai J, Yosef N, et al. Slingshot: cell lineage and pseudotime inference for single-cell transcriptomics. BMC Genomics 2018;19:477. https://doi.org/10.1186/s12864-018-4772-0.

[15] Fu J, Li K, Zhang W, Wan C, Zhang J, Jiang P, et al. Large-scale public data reuse to model immunotherapy response and resistance. Genome Med 2020;12:21. https://doi.org/10.1186/s13073-020-0721-z.

[16] Andreatta M, Corria-Osorio J, Müller S, Cubas R, Coukos G, Carmona SJ. Interpretation of T cell states from single-cell transcriptomics data using reference atlases. Nat Commun 2021;12:2965. https://doi.org/10.1038/s41467-021-23324-4.

[17] Higashi H, Maejima T, Lee LH, Yamazaki Y, Hottiger MO, Singh SA, et al. A Study into the ADP-Ribosylome of IFN-γ-Stimulated THP-1 Human Macrophage-like Cells Identifies ARTD8/PARP14 and ARTD9/PARP9 ADP-Ribosylation. J Proteome Res 2019;18:1607–22. https://doi.org/10.1021/acs.jproteome.8b00895.

[18] Lachmann A, Torre D, Keenan AB, Jagodnik KM, Lee HJ, Wang L, et al. Massive mining of publicly available RNA-seq data from human and mouse. Nat Commun 2018;9:1366. https://doi.org/10.1038/s41467-018-03751-6.
[19] Nathanson T, Ahuja A, Rubinsteyn A, Aksoy BA, Hellmann MD, Miao D, et al. Somatic Mutations and Neoepitope Homology in Melanomas Treated with CTLA-4 Blockade. Cancer Immunol Res 2017;5:84–91. https://doi.org/10.1158/2326-6066.CIR-16-0019.
[20] Mariathasan S, Turley SJ, Nickles D, Castiglioni A, Yuen K, Wang Y, et al. TGFβ attenuates tumour response to PD-L1 blockade by contributing to exclusion of T cells. Nature 2018;554:544–8. https://doi.org/10.1038/nature25501.
[21] Gide TN, Quek C, Menzies AM, Tasker AT, Shang P, Holst J, et al. Distinct Immune Cell Populations Define Response to Anti-PD-1 Monotherapy and Anti-PD-1/Anti-CTLA-4 Combined Therapy. Cancer Cell 2019;35:238-255.e6. https://doi.org/10.1016/j.ccell.2019.01.003.
[22] Wang X, Qiu L, Li Z, Wang X-Y, Yi H. Understanding the Multifaceted Role of Neutrophils in Cancer and Autoimmune Diseases. Front Immunol 2018;9. https://doi.org/10.3389/fimmu.2018.02456.
[23] Wherry EJ, Kurachi M. Molecular and cellular insights into T cell exhaustion. Nat Rev Immunol 2015;15:486–99. https://doi.org/10.1038/nri3862.
[24] Aibar S, González-Blas CB, Moerman T, Huynh-Thu VA, Imrichova H, Hulselmans G, et al. SCENIC: single-cell regulatory network inference and clustering. Nat Methods 2017;14:1083–6. https://doi.org/10.1038/nmeth.4463.
[25] Yuanhong X, Feng X, Qingchang L, Jianpeng F, Zhe L, Kejian G. Downregulation of Ap-1 Repressor Jdp2 is Associated with Tumor Metastasis and Poor Prognosis in Patients with Pancreatic Carcinoma. Int J Biol Markers 2010;25:136–40. https://doi.org/10.1177/172460081002500303.
[26] Atsaves V, Leventaki V, Rassidakis GZ, Claret FX. AP-1 Transcription Factors as Regulators of Immune Responses in Cancer. Cancers 2019;11:1037. https://doi.org/10.3390/cancers11071037.
[27] Iritani BM, Delrow J, Grandori C, Gomez I, Klacking M, Carlos LS, et al. Modulation of T-lymphocyte development, growth and cell size by the Myc antagonist and transcriptional repressor Mad1. EMBO J 2002;21:4820. https://doi.org/10.1093/emboj/cdf492.
[28] Lüscher B. MAD1 and its life as a MYC antagonist: An update. Eur J Cell Biol 2012;91:506–14. https://doi.org/10.1016/j.ejcb.2011.07.005.
[29] Kalfaoglu B, Almeida-Santos J, Tye CA, Satou Y, Ono M. T-Cell Hyperactivation and Paralysis in Severe COVID-19 Infection Revealed by Single-Cell Analysis. Front Immunol 2020;11. https://doi.org/10.3389/fimmu.2020.589380.
[30] Palmer DC, Webber BR, Patel Y, Johnson MJ, Kariya CM, Lahr WS, et al. Internal checkpoint regulates T cell neoantigen reactivity and susceptibility to PD1 blockade. Med 2022;3:682-704.e8. https://doi.org/10.1016/j.medj.2022.07.008.
[31] Avery L, Filderman J, Szymczak-Workman AL, Kane LP. Tim-3 co-stimulation promotes short-lived effector T cells, restricts memory precursors, and is dispensable for T cell exhaustion. Proc Natl Acad Sci 2018;115:2455–60. https://doi.org/10.1073/pnas.1712107115.
[32] Minnie SA, Waltner OG, Zhang P, Takahashi S, Nemychenkov NS, Ensbey KS, et al. TIM-3+ CD8 T cells with a terminally exhausted phenotype retain functional capacity in hematological malignancies. Sci Immunol 2024;9:eadg1094. https://doi.org/10.1126/sciimmunol.adg1094.

[33] Sestito C, Brevé JJP, Bol JGJM, Wilhelmus MMM, Drukarch B, van Dam A-M. Tissue Transglutaminase contributes to myelin phagocytosis in interleukin-4-treated human monocyte-derived macrophages. Cytokine 2020;128:155024. https://doi.org/10.1016/j.cyto.2020.155024.
[34] Liu Z, Kuang W, Zhou Q, Zhang Y. TGF-β1 secreted by M2 phenotype macrophages enhances the stemness and migration of glioma cells via the SMAD2/3 signalling pathway. Int J Mol Med 2018;42:3395. https://doi.org/10.3892/ijmm.2018.3923.
[35] Kloc M, Kubiak JZ, Zdanowski R, Ghobrial RM. Memory Macrophages. Int J Mol Sci 2022;24:38. https://doi.org/10.3390/ijms24010038.
[36] Zheng L, Han X, Yao S, Zhu Y, Klement J, Wu S, et al. The CD8α-PILRα interaction maintains CD8+ T cell quiescence. Science 2022;376:996–1001. https://doi.org/10.1126/science.aaz8658.
[37] Li Q, Yang Z, He X, Yang X. Comprehensive analysis of PILRA's association with the prognosis, tumor immune infiltration, and immunotherapy in pan-cancer. Sci Rep 2023;13:14334. https://doi.org/10.1038/s41598-023-41649-6.
[38] Huang AC, Zappasodi R. A decade of checkpoint blockade immunotherapy in melanoma: understanding the molecular basis for immune sensitivity and resistance. Nat Immunol 2022;23:660–70. https://doi.org/10.1038/s41590-022-01141-1.
[39] Rager T, Eckburg A, Patel M, Qiu R, Gantiwala S, Dovalovsky K, et al. Treatment of Metastatic Melanoma with a Combination of Immunotherapies and Molecularly Targeted Therapies. Cancers 2022;14:3779. https://doi.org/10.3390/cancers14153779.
[40] Wherry EJ, Kurachi M. Molecular and cellular insights into T cell exhaustion. Nat Rev Immunol 2015;15:486–99. https://doi.org/10.1038/nri3862.
[41] Collier JL, Weiss SA, Pauken KE, Sen DR, Sharpe AH. Not-so-opposite ends of the spectrum: CD8+ T cell dysfunction across chronic infection, cancer and autoimmunity. Nat Immunol 2021;22:809–19. https://doi.org/10.1038/s41590-021-00949-7.
[42] Sun Y, Caplazi P, Zhang J, Mazloom A, Kummerfeld S, Quinones G, et al. PILRα Negatively Regulates Mouse Inflammatory Arthritis. J Immunol 2014;193:860–70. https://doi.org/10.4049/jimmunol.1400045.
[43] Monroe K, Weerakkody T, Sabelström H, Tatarakis D, Suh J, Chin M, et al. PILRA regulates microglial neuroinflammation and lipid metabolism as a candidate therapeutic target for Alzheimer's disease 2024. https://doi.org/10.21203/rs.3.rs-3954863/v1.
[44] Wang H, Yung MMH, Ngan HYS, Chan KKL, Chan DW. The Impact of the Tumor Microenvironment on Macrophage Polarization in Cancer Metastatic Progression. Int J Mol Sci 2021;22:6560. https://doi.org/10.3390/ijms22126560.
[45] Chen S, Saeed AFUH, Liu Q, Jiang Q, Xu H, Xiao GG, et al. Macrophages in immunoregulation and therapeutics. Signal Transduct Target Ther 2023;8:207. https://doi.org/10.1038/s41392-023-01452-1.
[46] Sica A, Erreni M, Allavena P, Porta C. Macrophage polarization in pathology. Cell Mol Life Sci 2015;72:4111–26. https://doi.org/10.1007/s00018-015-1995-y.
[47] Mantovani A, Marchesi F, Malesci A, Laghi L, Allavena P. Tumour-associated macrophages as treatment targets in oncology. Nat Rev Clin Oncol 2017;14:399–416. https://doi.org/10.1038/nrclinonc.2016.217.
[48] Qian B-Z, Pollard JW. Macrophage Diversity Enhances Tumor Progression and Metastasis. Cell 2010;141:39–51. https://doi.org/10.1016/j.cell.2010.03.014.

[49] Zhang Y, Guan X, Jiang P. Cytokine and Chemokine Signals of T-Cell Exclusion in Tumors. Front Immunol 2020;11. https://doi.org/10.3389/fimmu.2020.594609.
[50] Kohli K, Pillarisetty VG, Kim TS. Key chemokines direct migration of immune cells in solid tumors. Cancer Gene Ther 2022;29:10–21. https://doi.org/10.1038/s41417-021-00303-x.
[51] Mehrotra P, Krishnamurthy P, Sun J, Goenka S, Kaplan MH. Poly-ADP-ribosyl polymerase-14 promotes T helper 17 and follicular T helper development. Immunology 2015;146:537–46. https://doi.org/10.1111/imm.12515.
[52] Mehrotra P, Riley JP, Patel R, Li F, Voss L, Goenka S. PARP-14 Functions as a Transcriptional Switch for Stat6-dependent Gene Activation. J Biol Chem 2011;286:1767–76. https://doi.org/10.1074/jbc.M110.157768.
[53] Bennett TJ, Udupa VAV, Turner SJ. Running to Stand Still: Naive CD8+ T Cells Actively Maintain a Program of Quiescence. Int J Mol Sci 2020;21:9773. https://doi.org/10.3390/ijms21249773.
[54] Anderson KG, Stromnes IM, Greenberg PD. Obstacles Posed by the Tumor Microenvironment to T cell Activity: A Case for Synergistic Therapies. Cancer Cell 2017;31:311–25. https://doi.org/10.1016/j.ccell.2017.02.008.
[55] Yang L, Li A, Lei Q, Zhang Y. Tumor-intrinsic signaling pathways: key roles in the regulation of the immunosuppressive tumor microenvironment. J Hematol OncolJ Hematol Oncol 2019;12:125. https://doi.org/10.1186/s13045-019-0804-8.
[56] Liu Z, Yu X, Xu L, Li Y, Zeng C. Current insight into the regulation of PD-L1 in cancer. Exp Hematol Oncol 2022;11:44. https://doi.org/10.1186/s40164-022-00297-8.
[57] Castro F, Cardoso AP, Gonçalves RM, Serre K, Oliveira MJ. Interferon-Gamma at the Crossroads of Tumor Immune Surveillance or Evasion. Front Immunol 2018;9. https://doi.org/10.3389/fimmu.2018.00847.

Figure 1 – Identification of a genetic signature associated with PARP14 inhibition.
YUMM2.1 and 501MEL cells treated for 48h *in vitro* with either DMSO, 100nM PARP14 inhibitor (RBN012759), or 500nM PARP14 PROTAC (RBN012811); $n = 3$. **A.** Bulk RNAseq analysis of a PARP14 inhibition signature identified across human and mouse cell lines. Heatmap of treatment vs control per cell line, colours representing row-scaled z-score expression high (red) to low (blue). **B.** Gene set enrichment analysis (GSEA) of 30 PARP14i signature genes identified by comparison of bulk RNAseq from human and mouse cell lines, chronically treated with IFN-γ followed by 48 hours of PARP14 inhibition (Metascape analysis, values presented as $-\log_{10}$ of P value). **C.** Kaplan-Meier (KM) curves showing cancer patients with high Tumour Immune Dysfunction and Exclusion (TIDE) scores of PARP14i signature genes having better overall survival (OS) rates in representative studies. Red indicates patients with high (top 50%) TIDE scores and blue indicates low (bottom 50%) TIDE scores. **D.** Bulk RNAseq analysis on naïve YUMM2.1 tumours treated with IgG or α-PD-1. α-PD-1-treated cohort was split into relapsed and responders. Compared to YUMM2.1 tumours pre-treated with chronic IFN-γ stimulation.

Figure 2 – Analysis of the cellular composition of YUMM2.1 tumours relapsing following α-PD-1 antibodies with and without PARP14 inhibitor treatment. **A.** YUMM2.1 cells were implanted subcutaneously into the flank of female C57BL/6 mice. Once

tumours reached ~80mm^3 in volume, treatment of α-PD-1 antibodies was commenced for a total of two doses, 3 days apart. Tumour shrinkage and regrowth was monitored. When tumours reached a volume between ~100-150mm^3, a second round of treatment commenced, lasting 7 days. Tumours were subsequently processed for single-cell RNAseq. Graphical summary of experimental timeline, showing tumour inoculation and treatment regime (top), and illustration of tumour growth (bottom). **B.** Mutual nearest neighbour (MNN) corrected Uniform Manifold Approximation and Projection (UMAP) of 13 tumour samples (*n*=65,476 cells). Clustered using Leiden unsupervised clustering and coloured by cell types. Cluster identifies below. **C.** Cell number changes in each cluster by treatment: three mice IgG2a; three mice α-PD-1; three mice PARP14i (RBN012759) alone; and four mice a combination of α-PD-1 + PARP14i (RBN012759). **D.** Cell density projections by treatment.

Figure 4 - PARP14 inhibitor treatment in combination with α-PD-1 therapy drives activated cytotoxic T cells but limits transition to dysfunctional states. **A.** MNN corrected UMAP of T cell and natural killer (NK) cells (clusters 12-17, *n=18,298*). Subclustered using Louvain method of community ordering and coloured by subclusters. **B.** Cell number changes in each T and NK cell subcluster by treatment: IgG2a; α-PD-1; PARP14i (RBN012759); combination treatment α-PD-1 + PARP14i (RBN012759). **C.** Cell density projections of T and NK cells by treatment. **D.** T cell subcluster identity- clusters 13-16. GSEA relevant terms of up- (red, FDR=0.05, top 25 genes) and downregulated (blue, FDR=0.05, bottom 25 genes) genes (Metascape analysis, values presented as -log$_{10}$ of P value). **E.** Gene expression presented as high (red) to low (blue) average expression and ratio of cells expressing (circle size), across T cell subclusters 13-16. **F.** Slingshot trajectory inference analysis of CD8$^+$ T cell subclusters 13-18 (*n=6,194*) with trajectory direction indicated by arrows (black). **G.** KM curves showing cancer patients with high TIDE scores of genes from T cell subclusters 13-16 and their effect on OS rates in bladder cancer cohort. Red indicates patients with high (top 50%) TIDE scores and blue indicates low (bottom 50%) TIDE scores. **H.** Binarised heatmap of each T cell subcluster by relative regulon activity (SCENIC analysis). **I - N.** Flow cytometry analysis of YUMM2.1 tumour xenografts in C57BL/6 mice relapsing on an initial dose of α-PD-1 and harvested on-treatment following subsequent dosing with either α-PD-1 (Blue; *n* = 6) or α-PD-1 + PARP14i (Red; *n* = 6). **I.** Percentage of total immune cells and individual T cell subsets as a proportion of CD45$^+$ cells. **J.** Percentage of cytotoxic CD8$^+$ T cells evaluated via their expression of GZMB. Percentage of exhaustion subsets in cytotoxic T cells measured by LAG-3 and TIM-3 levels for PD-1$^+$ **(K)**, PD-1$^+$CTLA-4$^+$ **(L)**, or PD-1$^+$CTLA-4$^-$ **(M)** background. The p-value was assessed by two-sided unpaired t-test and the data were presented as the mean±SEM. **p*0.05, ****p*<0.01, ****p*<0.001, *****p*<0.0001.

Figure 5 - PARP14 inhibitor treatment increases M1 macrophage polarisation to generate a memory-like state. **A.** MNN corrected UMAP of monocytes and macrophages (clusters 1-8, *n*=34,705). Subclustered using Louvain method of community ordering and coloured by subclusters. **B.** Cell number changes in each subcluster by treatment: IgG2a; α-PD-1; PARP14i (RBN012759); combination treatment α-PD-1 + PARP14i (RBN012759). **C.** Cell density projections of both monocytes and macrophages (colloquially referred to as MonoMacs) by treatment. **D.** Macrophage

subcluster identity- subclusters 2, 4, 8 and 10. GSEA of up- (FDR=0.05, logFC > 1, marked in red) and downregulated (FDR=0.05, logFC < -1, marked in blue) genes (Metascape analysis, values presented as -$\log_{10}$ of P value). **E.** Gene expression presented as high (red) to low (blue) average expression and ratio of cells expressing (circle size), across Macrophage subclusters. **F.** Binarised heatmap of 10% random subsampling of each MonoMac subcluster by relative regulon activity (SCENIC analysis).

#

A. YUMM2.1 cells were implanted subcutaneously into the flank of female C57BL/6 mice. Once tumours reached ~80mm^3 in volume, treatment of α-PD-1 antibodies was commenced for a total of two doses, 3 days apart. Tumour shrinkage and regrowth was monitored. When tumours reached a volume between ~100-150mm^3, a second round of treatment commenced, lasting 7 days. Tumours were subsequently processed for single-cell RNAseq. Graphical summary of experimental timeline, showing tumour inoculation and treatment regime (top), and illustration of tumour growth (bottom). **B.** Mutual nearest neighbour (MNN) corrected Uniform Manifold Approximation and Projection (UMAP) of 13 tumour samples (*n*=65,476 cells). Clustered using Leiden unsupervised clustering and coloured by cell types. Cluster identifies below. **C.** Cell number changes in each cluster by treatment: three mice IgG2a; three mice α-PD-1; three mice PARP14i (RBN012759) alone; and four mice a combination of α-PD-1 + PARP14i (RBN012759). **D.** Cell density projections by treatment.

Figure 3 - PARP14 inhibitor treatment in combination with α-PD-1 therapy drives activated cytotoxic T cells but limits transition to dysfunctional states. **A.** MNN corrected UMAP of T cell and natural killer (NK) cells (clusters 12-17, *n=18,298*). Subclustered using Louvain method of community ordering and coloured by subclusters. **B.** Cell number changes in each T and NK cell subcluster by treatment: IgG2a; α-PD-1; PARP14i (RBN012759); combination treatment α-PD-1 + PARP14i (RBN012759). **C.** Cell density projections of T and NK cells by treatment. **D.** T cell subcluster identity- clusters 13-16. GSEA relevant terms of up- (red, FDR=0.05, top 25 genes) and downregulated (blue, FDR=0.05, bottom 25 genes) genes (Metascape analysis, values presented as -$\log_{10}$ of P value). **E.** Gene expression presented as high (red) to low (blue) average expression and ratio of cells expressing (circle size), across T cell subclusters 13-16. **F.** Slingshot trajectory inference analysis of CD8$^+$ T cell subclusters 13-18 (*n=6,194*) with trajectory direction indicated by arrows (black). **G.** KM curves showing cancer patients with high TIDE scores of genes from T cell subclusters 13-16 and their effect on OS rates in bladder cancer cohort. Red indicates patients with high (top 50%) TIDE scores and blue indicates low (bottom 50%) TIDE scores. **H.** Binarised heatmap of each T cell subcluster by relative regulon activity (SCENIC analysis). **I - N.** Flow cytometry analysis of YUMM2.1 tumour xenografts in C57BL/6 mice relapsing on an initial dose of α-PD-1 and harvested on-treatment following subsequent dosing with either α-PD-1 (Blue; *n* = 6) or α-PD-1 + PARP14i (Red; *n* = 6). **I.** Percentage of total immune cells and individual T cell subsets as a proportion of CD45$^+$ cells. **J.** Percentage of cytotoxic CD8$^+$ T cells evaluated via their expression of GZMB. Percentage of exhaustion subsets in cytotoxic T cells measured by LAG-3 and TIM-3 levels for PD-1$^+$ **(K)**, PD-1$^+$CTLA-4$^+$ **(L)**, or PD-1$^+$CTLA-4$^-$ **(M)** background. The p-value was assessed by two-sided unpaired t-test and the data were presented as the mean ± SEM. *$p < 0.05$, ***$p < 0.01$, ***$p < 0.001$, ****$p < 0.0001$.

Figure 4 - PARP14 inhibitor treatment increases M1 macrophage polarisation to generate a memory-like state.

A. MNN corrected UMAP of monocytes and macrophages (clusters 1-8, *n*=34,705). Subclustered using Louvain method of community ordering and coloured by subclusters. **B.** Cell number changes in each subcluster by treatment: IgG2a; α-PD-1; PARP14i (RBN012759); combination treatment α-PD-1 + PARP14i (RBN012759). **C.** Cell density projections of both monocytes and macrophages (colloquially referred to as MonoMacs) by treatment. **D.** Macrophage subcluster identity- subclusters 2, 4, 8 and 10. GSEA of up- (FDR=0.05, logFC > 1, marked in red) and downregulated (FDR=0.05, logFC < -1, marked in blue) genes (Metascape analysis, values presented as -$\log_{10}$ of P value). **E.** Gene expression presented as high (red) to low (blue) average expression and ratio of cells expressing (circle size), across Macrophage subclusters. **F.** Binarised heatmap of 10% random subsampling of each MonoMac subcluster by relative regulon activity (SCENIC analysis).

Figure 5 - Combined treatment of α-PD-1 with PARP14 inhibitor promotes dynamic adaptive resistance strategies in tumour cells which permit their persistence.

A. MNN corrected UMAP of tumour and cancer associated fibroblasts (CAFs) cells (clusters 26-28, *n=3,445*). Subclustered using Louvain method of community ordering and coloured by subclusters. **B.** Cell number changes in each subcluster by treatment: IgG2a; α-PD-1; PARP14i (RBN012759); combination treatment α-PD-1 + PARP14i (RBN012759). **C.** Cell density projections of tumour and CAF cells by treatment. **D.** Slingshot trajectory inference analysis of tumour cells with trajectory direction indicated by arrows (black). **E.** Tumour subcluster identity, GSEA relevant terms of up- (red, FDR=0.05, logFC > 1) and downregulated (blue, FDR=0.05, logFC < -1) genes in tumour subclusters 1-4 (Metascape analysis, values presented as -$\log_{10}$ of P value). **F.** PARP14i signature gene expression presented as high (red) to low (blue) average expression and ratio of cells expressing (circle size), across tumour and CAF subclusters in different treatments.

Supplementary Figure 1 – Identification of a genetic signature associated with PARP14 inhibition.

MC38 or A375 cells treated for 48h *in vitro* with either DMSO, 100nM PARP14 inhibitor (RBN012759), or 500nM PARP14 PROTAC (RBN012811); *n* = 3. Bulk RNAseq analysis of a PARP14 inhibition signature identified across human and mouse cell lines. Heatmap of treatment vs control per cell line, colours representing row-scaled z-score expression high (red) to low (blue).

Supplementary Figure 2 –

Clustergram of gene-TF associations derived from EnrichR analysis using the ARCHS4_TFs_Coexp database. Heatmap displays associations between genes (rows) and transcription factor terms (columns). Colour-coded to represent the -log10 transformed adjusted p-values of enrichment, darker colours indicating stronger statistical significance. No normalisation is applied, ensuring raw association strengths are visualised.

Supplementary Figure 3 -

A. YUMM2.1 cells were implanted subcutaneously into the flank of female C57BL/6 mice. Once tumours reached ~80mm^3 in volume, treatment of α-PD-1 antibodies was commenced for a total of two doses, 3 days apart (horizontal dotted line). Tumour shrinkage and regrowth was monitored and individual growth curves plotted. When tumours reached a volume between ~100-150mm^3, a second round of treatment commenced (day 0); consisting of four IgG2a, α-PD-1, PARP14i or a combination of α-PD-1 + PARP14i. Treatment lasted 7 days. Tumours were subsequently processed for single-cell RNAseq. **B.** RNAseq data of excluded IgG2a control treated tumour sample (black triangles and high-density lines) projected on the sample UMAP (colour) using projecTILs R package. **C.** Sample representation in each cluster **–** histogram and **D.** UMAP. **E.** Cell number changes in each cell type by treatment: three mice IgG2a; three mice α-PD-1; three mice PARP14i (RBN012759) alone; and four mice a combination of α-PD-1 + PARP14i (RBN012759).

Supplementary Figure 4 – -

A. Bulk RNAseq analysis on naïve YUMM2.1 tumours treated with IgG or α-PD-1. α-PD-1-treated cohort was split into relapsed and responders. Compared to YUMM2.1 tumours pre-treated with chronic IFN-γ stimulation. Heatmap representations of uniquely upregulated genes per each subcluster within the top 200 expressed genes. Boxes represent relevant clinical outcome per cluster. **B.** KM curves showing cancer patients with high TIDE scores of uniquely upregulated genes per tumour subcluster and their effect on OS rates in bladder cancer cohort. Red indicates patients with high (top 50%) TIDE scores and blue indicates low (bottom 50%) TIDE scores.

Supplementary Figure 5

A. Selected T cell marker gene expression presented as high (red) to low (blue) average expression and ratio of cells expressing (circle size), across T cell subclusters. **B.** Bulk RNAseq analysis on naïve YUMM2.1 tumours treated with IgG or α-PD-1. α-PD-1-treated cohort was split into relapsed and responders. Compared to YUMM2.1 tumours pre-treated with chronic IFN-γ stimulation. Heatmap representations of activation and exhaustion markers. **C.** Representative image of Arid3a, Cebpb, Irf5, Mxd1 regulon activity AUC score in MNN corrected T cell subcluster UMAP. Calculated by SCENIC. **D.** Binarised heatmap of CD8$^+$ T cell subclusters by relative regulon activity (SCENIC analysis).

Supplementary Figure 6 – Flow cytometry gating strategy for T cell subsets and exhaustion phenotypes

Supplementary Figure 5 – Flow cytometry gating strategy for T cell subsets and exhaustion phenotypes

Supplementary Figure 6 –

A. Bulk RNAseq analysis on naïve YUMM2.1 tumours treated with IgG or α-PD-1. α-PD-1-treated cohort was split into relapsed and responders. Compared to YUMM2.1 tumours pre-treated with chronic IFN-γ stimulation. Heatmap representations of uniquely upregulated genes per each subcluster within the top 200 expressed genes. Boxes represent relevant clinical outcome per cluster. **B.** KM curves showing cancer patients with high TIDE scores of uniquely upregulated genes per tumour subcluster and their effect on OS rates

in bladder cancer cohort. Red indicates patients with high (top 50%) TIDE scores and blue indicates low (bottom 50%) TIDE scores.

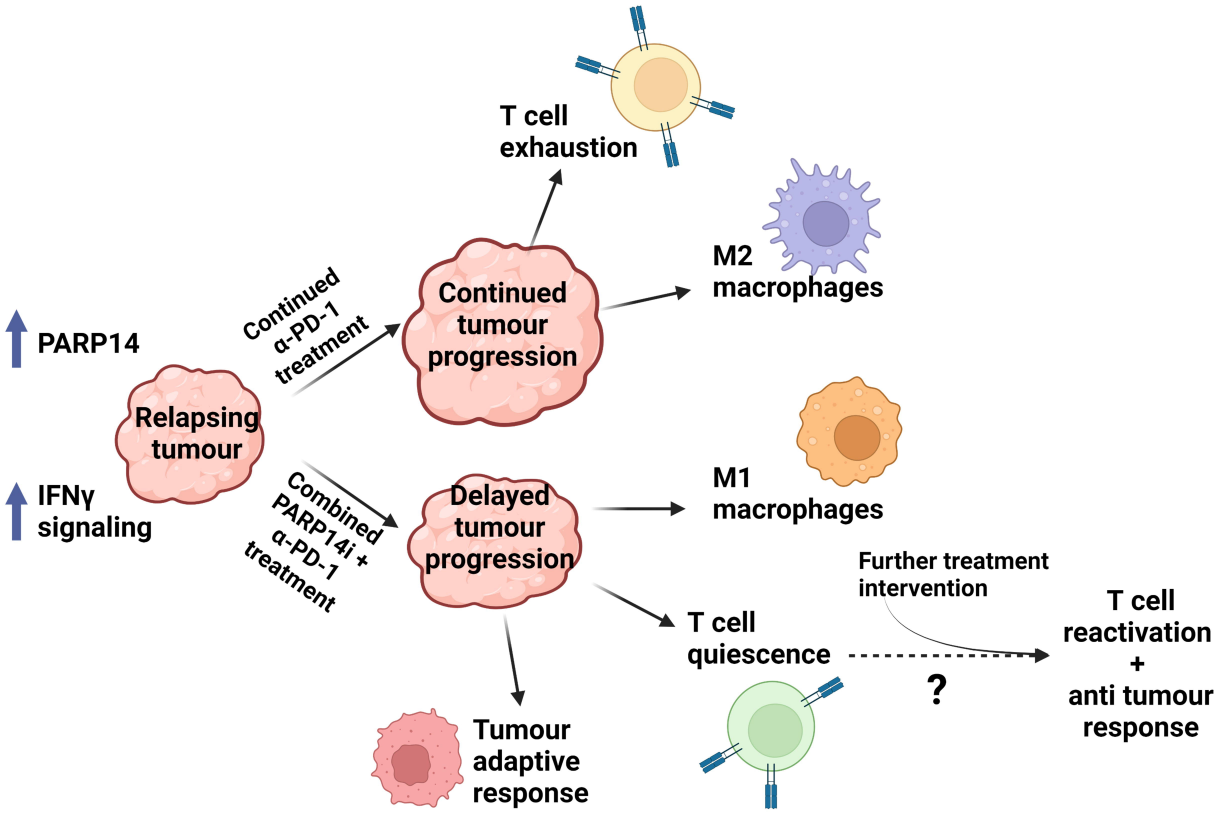
T cell
exhaustion
M2
macrophages
PARP14
Continued
α-PD-1
treatment
Continued
tumour
progression
Relapsing
tumour
IFNγ
signaling
Combined
PARP14i +
α-PD-1
treatment
Delayed
tumour
progression
M1
macrophages
Further treatment
intervention
T cell
quiescence
?
T cell
reactivation
+
anti tumour
response
Tumour
adaptive
response

Fig 1

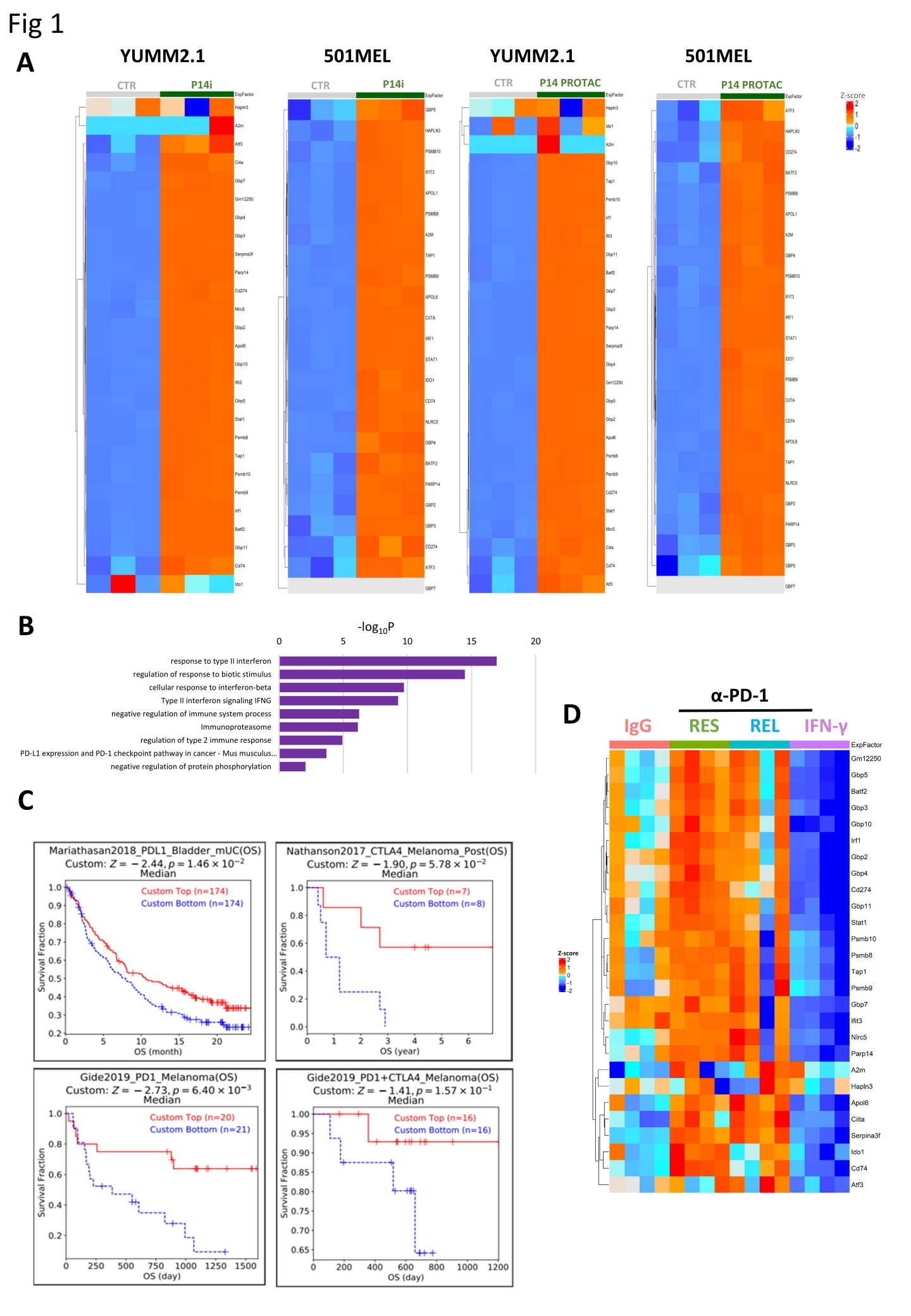
A
YUMM2.1
501MEL
YUMM2.1
501MEL
CTR
P14i
CTR
P14i
CTR
P14 PROTAC
CTR
P14 PROTAC
ExpFactor
Z-score
B
-log10P
0
5
10
15
20
response to type II interferon
regulation of response to biotic stimulus
cellular response to interferon-beta
Type II interferon signaling IFNG
negative regulation of immune system process
Immunoproteasome
regulation of type 2 immune response
PD-L1 expression and PD-1 checkpoint pathway in cancer - Mus musculus...
negative regulation of protein phosphorylation
C
Mariathasan2018_PDL1_Bladder_mUC(OS)
Custom: Z = −2.44, p = 1.46 × 10−2
Median
Custom Top (n=174)
Custom Bottom (n=174)
Survival Fraction
OS (month)
Nathanson2017_CTLA4_Melanoma_Post(OS)
Custom: Z = −1.90, p = 5.78 × 10−2
Median
Custom Top (n=7)
Custom Bottom (n=8)
Survival Fraction
OS (year)
Gide2019_PD1_Melanoma(OS)
Custom: Z = −2.73, p = 6.40 × 10−3
Median
Custom Top (n=20)
Custom Bottom (n=21)
Survival Fraction
OS (day)
Gide2019_PD1+CTLA4_Melanoma(OS)
Custom: Z = −1.41, p = 1.57 × 10−1
Median
Custom Top (n=16)
Custom Bottom (n=16)
Survival Fraction
OS (day)
D
α-PD-1
IgG
RES
REL
IFN-γ
ExpFactor
Z-score
Gm12250
Gbp5
Batf2
Gbp3
Gbp10
Irf1
Gbp2
Gbp4
Cd274
Gbp11
Stat1
Psmb10
Psmb8
Tap1
Psmb9
Gbp7
Ifit3
Nlrc5
Parp14
A2m
Hapln3
Apol6
Ciita
Serpina3f
Ido1
Cd74
Atf3

Fig 2

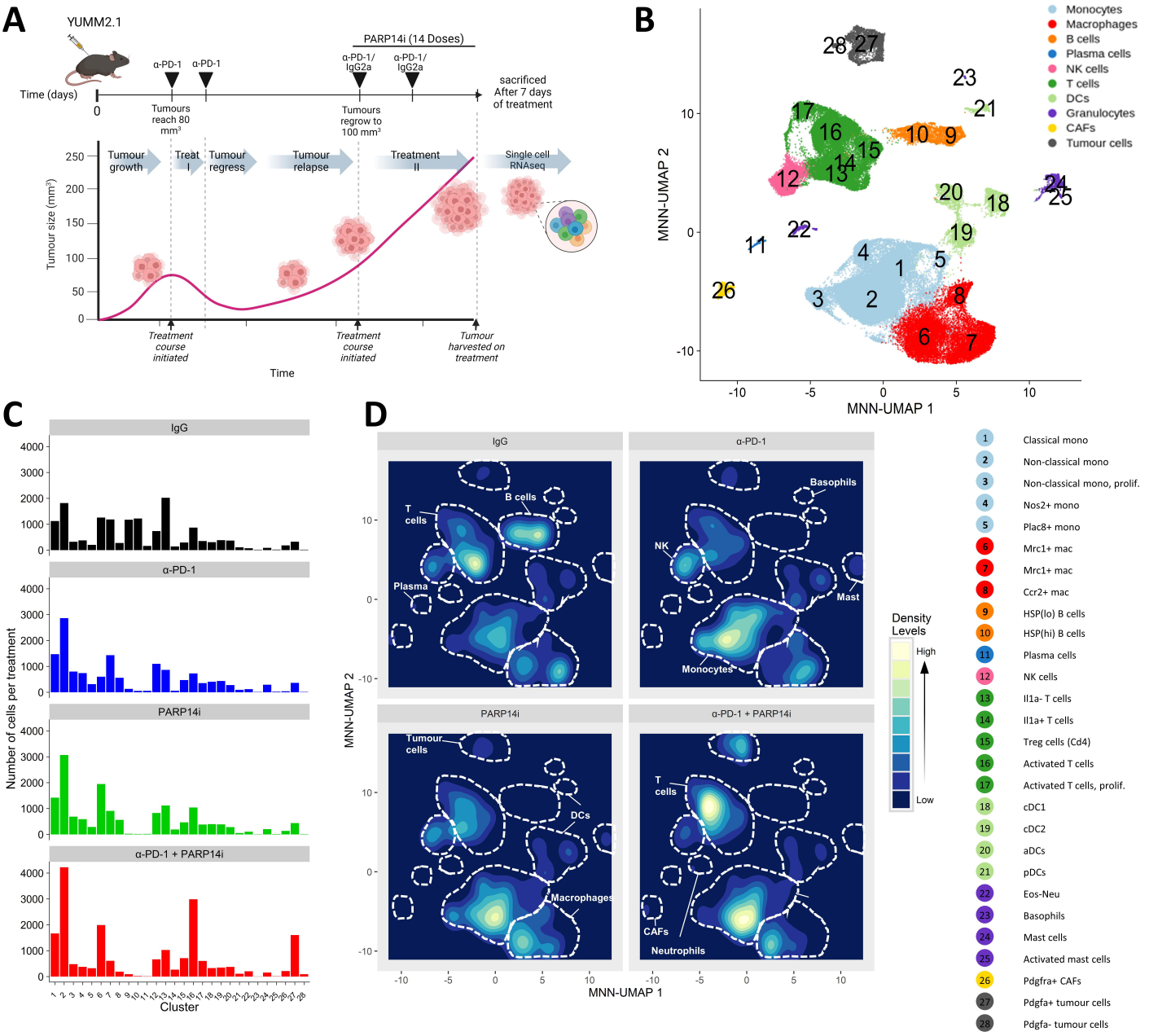
A
YUMM2.1
Time (days)
0
α-PD-1
α-PD-1
Tumours reach 80 mm³
PARP14i (14 Doses)
α-PD-1/ IgG2a
α-PD-1/ IgG2a
Tumours regrow to 100 mm³
sacrificed After 7 days of treatment
Tumour growth
Treat I
Tumour regress
Tumour relapse
Treatment II
Single cell RNAseq
Tumour size (mm³)
Treatment course initiated
Treatment course initiated
Tumour harvested on treatment
Time
B
Monocytes
Macrophages
B cells
Plasma cells
NK cells
T cells
DCs
Granulocytes
CAFs
Tumour cells
MNN-UMAP 2
MNN-UMAP 1
C
IgG
α-PD-1
PARP14i
α-PD-1 + PARP14i
Number of cells per treatment
Cluster
D
IgG
α-PD-1
PARP14i
α-PD-1 + PARP14i
T cells
B cells
Plasma
Basophils
NK
Mast
Monocytes
Tumour cells
DCs
Macrophages
CAFs
Neutrophils
Density Levels
High
Low
MNN-UMAP 2
MNN-UMAP 1
1 Classical mono
2 Non-classical mono
3 Non-classical mono, prolif.
4 Nos2+ mono
5 Plac8+ mono
6 Mrc1+ mac
7 Mrc1+ mac
8 Ccr2+ mac
9 HSP(lo) B cells
10 HSP(hi) B cells
11 Plasma cells
12 NK cells
13 Il1a- T cells
14 Il1a+ T cells
15 Treg cells (Cd4)
16 Activated T cells
17 Activated T cells, prolif.
18 cDC1
19 cDC2
20 aDCs
21 pDCs
22 Eos-Neu
23 Basophils
24 Mast cells
25 Activated mast cells
26 Pdgfra+ CAFs
27 Pdgfa+ tumour cells
28 Pdgfa- tumour cells

Fig 3

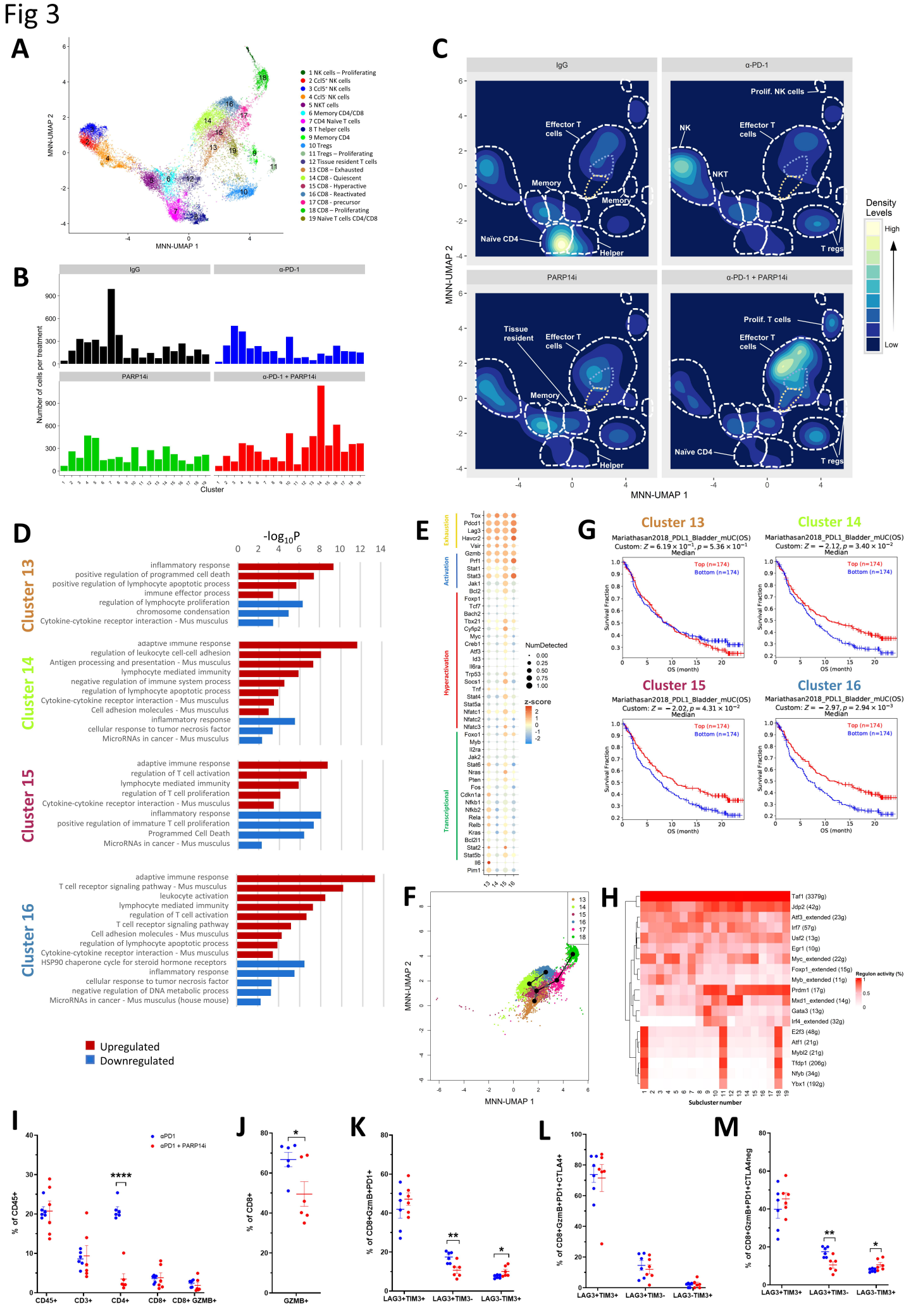
A
MNN-UMAP 1
MNN-UMAP 2
1 NK cells – Proliferating
2 Ccl5+ NK cells
3 Ccl5+ NK cells
4 Ccl5- NK cells
5 NKT cells
6 Memory CD4/CD8
7 CD4 Naïve T cells
8 T helper cells
9 Memory CD4
10 Tregs
11 Tregs – Proliferating
12 Tissue resident T cells
13 CD8 – Exhausted
14 CD8 - Quiescent
15 CD8 - Hyperactive
16 CD8 - Reactivated
17 CD8 - precursor
18 CD8 – Proliferating
19 Naïve T cells CD4/CD8
B
IgG
α-PD-1
PARP14i
α-PD-1 + PARP14i
Number of cells per treatment
Cluster
C
IgG
α-PD-1
PARP14i
α-PD-1 + PARP14i
Effector T cells
Memory
Naïve CD4
Helper
Prolif. NK cells
NK
NKT
T regs
Tissue resident
Prolif. T cells
Density Levels
High
Low
MNN-UMAP 1
MNN-UMAP 2
D
-log10P
Cluster 13
inflammatory response
positive regulation of programmed cell death
positive regulation of lymphocyte apoptotic process
immune effector process
regulation of lymphocyte proliferation
chromosome condensation
Cytokine-cytokine receptor interaction - Mus musculus
Cluster 14
adaptive immune response
regulation of leukocyte cell-cell adhesion
Antigen processing and presentation - Mus musculus
lymphocyte mediated immunity
negative regulation of immune system process
regulation of lymphocyte apoptotic process
Cytokine-cytokine receptor interaction - Mus musculus
Cell adhesion molecules - Mus musculus
inflammatory response
cellular response to tumor necrosis factor
MicroRNAs in cancer - Mus musculus
Cluster 15
adaptive immune response
regulation of T cell activation
lymphocyte mediated immunity
regulation of T cell proliferation
Cytokine-cytokine receptor interaction - Mus musculus
inflammatory response
positive regulation of immature T cell proliferation
Programmed Cell Death
MicroRNAs in cancer - Mus musculus
Cluster 16
adaptive immune response
T cell receptor signaling pathway - Mus musculus
leukocyte activation
lymphocyte mediated immunity
regulation of T cell activation
T cell receptor signaling pathway
Cell adhesion molecules - Mus musculus
regulation of lymphocyte apoptotic process
Cytokine-cytokine receptor interaction - Mus musculus
HSP90 chaperone cycle for steroid hormone receptors
inflammatory response
cellular response to tumor necrosis factor
negative regulation of DNA metabolic process
MicroRNAs in cancer - Mus musculus (house mouse)
Upregulated
Downregulated
E
Exhaustion
Activation
Hyperactivation
Transcriptional
NumDetected
z-score
F
MNN-UMAP 1
MNN-UMAP 2
G
Cluster 13
Cluster 14
Cluster 15
Cluster 16
Mariathasan2018_PDL1_Bladder_mUC(OS)
Median
Top (n=174)
Bottom (n=174)
Survival Fraction
OS (month)
H
Regulon activity (%)
Subcluster number
I
αPD1
αPD1 + PARP14i
% of CD45+
CD45+
CD3+
CD4+
CD8+
CD8+ GZMB+
J
% of CD8+
GZMB+
K
% of CD8+GzmB+PD1+
LAG3+TIM3+
LAG3+TIM3-
LAG3-TIM3+
L
% of CD8+GzmB+PD1+CTLA4+
M
% of CD8+GzmB+PD1+CTLA4neg

Fig 4

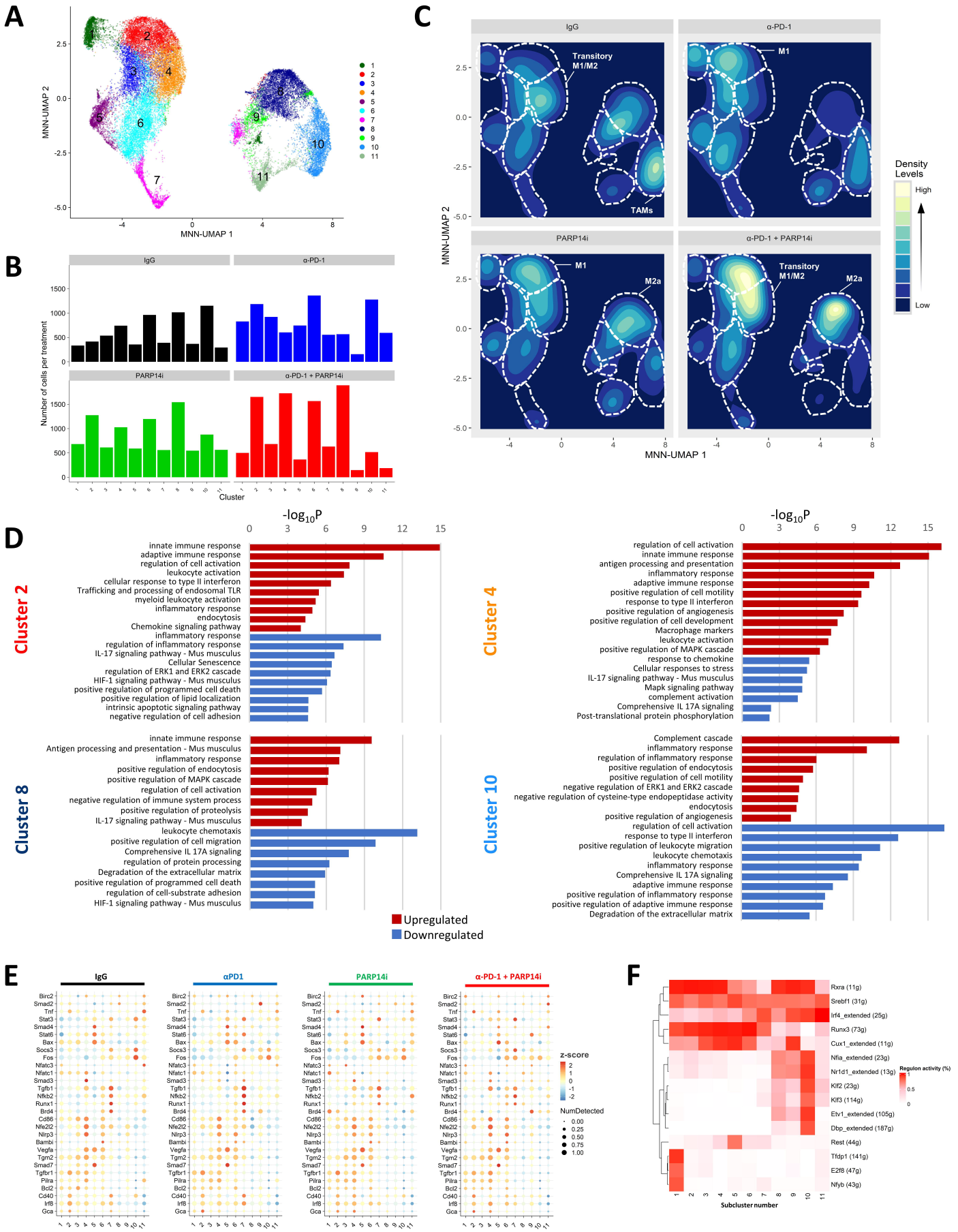
A
MNN-UMAP 1
MNN-UMAP 2
B
IgG
α-PD-1
PARP14i
α-PD-1 + PARP14i
Number of cells per treatment
Cluster
C
Transitory M1/M2
M1
TAMs
M2a
Density Levels
High
Low
D
-log10P
Cluster 2
Cluster 4
Cluster 8
Cluster 10
Upregulated
Downregulated
E
IgG
αPD1
PARP14i
α-PD-1 + PARP14i
z-score
NumDetected
F
Rxra (11g)
Srebf1 (31g)
Irf4_extended (25g)
Runx3 (73g)
Cux1_extended (11g)
Nfia_extended (23g)
Nr1d1_extended (13g)
Klf2 (23g)
Klf3 (114g)
Etv1_extended (105g)
Dbp_extended (187g)
Rest (44g)
Tfdp1 (141g)
E2f8 (47g)
Nfyb (43g)
Regulon activity (%)
Subcluster number

Fig 5

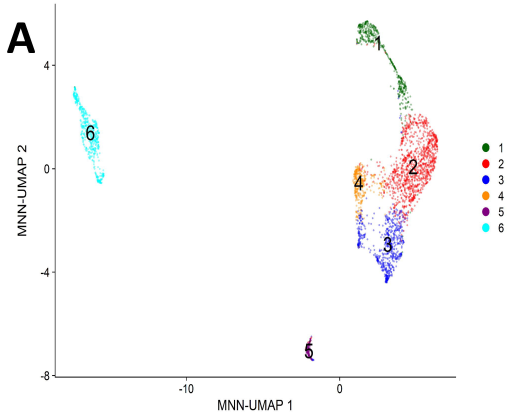
A
MNN-UMAP 2
MNN-UMAP 1
1
2
3
4
5
6

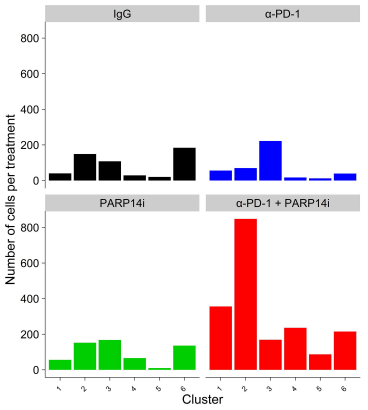
B
IgG
α-PD-1
PARP14i
α-PD-1 + PARP14i
Number of cells per treatment
Cluster

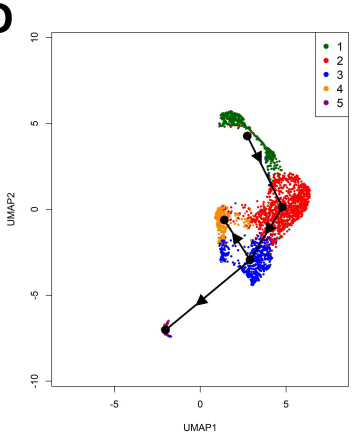
D
UMAP2
UMAP1
1
2
3
4
5

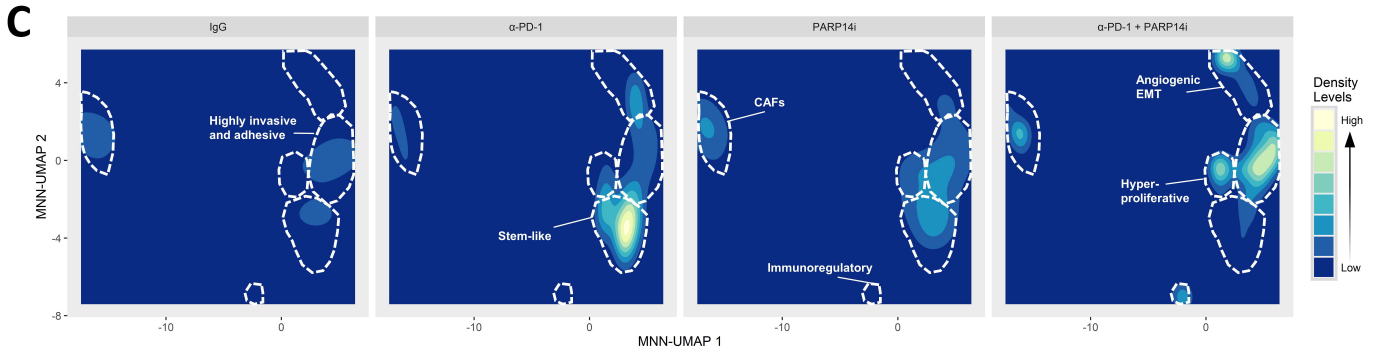
C
IgG
α-PD-1
PARP14i
α-PD-1 + PARP14i
Highly invasive and adhesive
Stem-like
CAFs
Immunoregulatory
Angiogenic EMT
Hyper-proliferative
Density Levels
High
Low
MNN-UMAP 2
MNN-UMAP 1

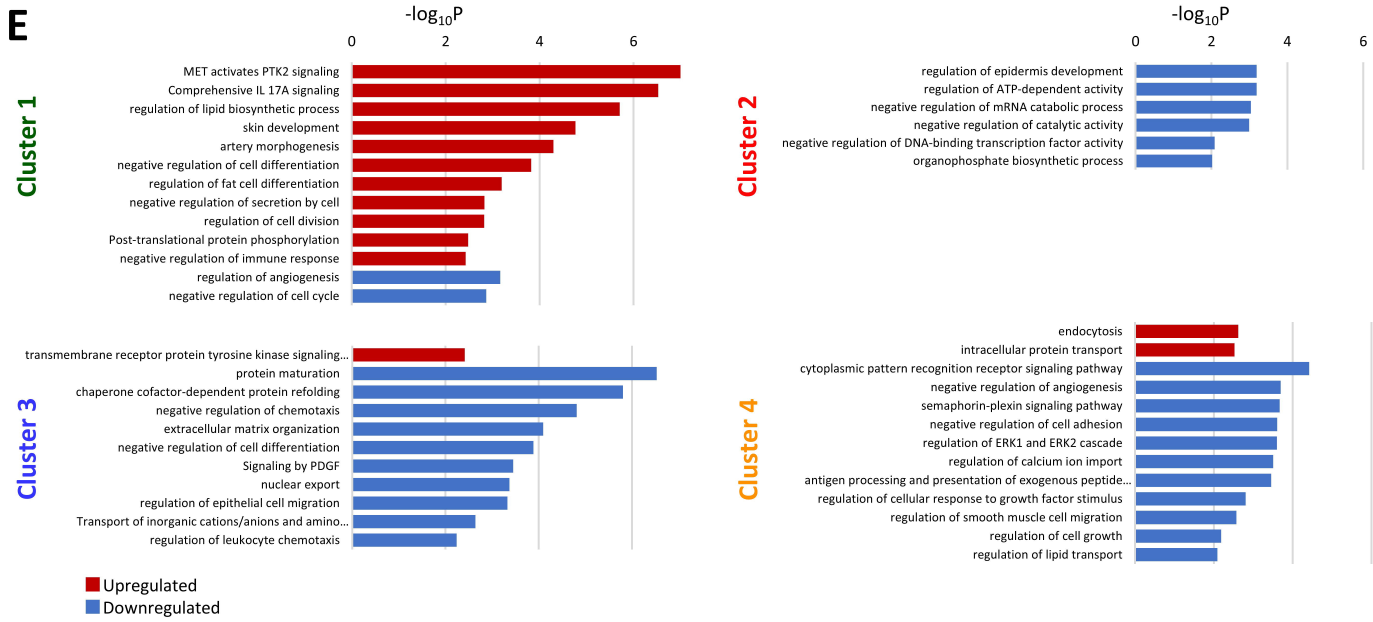
E
-log10P
Cluster 1
MET activates PTK2 signaling
Comprehensive IL 17A signaling
regulation of lipid biosynthetic process
skin development
artery morphogenesis
negative regulation of cell differentiation
regulation of fat cell differentiation
negative regulation of secretion by cell
regulation of cell division
Post-translational protein phosphorylation
negative regulation of immune response
regulation of angiogenesis
negative regulation of cell cycle
Cluster 2
regulation of epidermis development
regulation of ATP-dependent activity
negative regulation of mRNA catabolic process
negative regulation of catalytic activity
negative regulation of DNA-binding transcription factor activity
organophosphate biosynthetic process
Cluster 3
transmembrane receptor protein tyrosine kinase signaling...
protein maturation
chaperone cofactor-dependent protein refolding
negative regulation of chemotaxis
extracellular matrix organization
negative regulation of cell differentiation
Signaling by PDGF
nuclear export
regulation of epithelial cell migration
Transport of inorganic cations/anions and amino...
regulation of leukocyte chemotaxis
Cluster 4
endocytosis
intracellular protein transport
cytoplasmic pattern recognition receptor signaling pathway
negative regulation of angiogenesis
semaphorin-plexin signaling pathway
negative regulation of cell adhesion
regulation of ERK1 and ERK2 cascade
regulation of calcium ion import
antigen processing and presentation of exogenous peptide...
regulation of cellular response to growth factor stimulus
regulation of smooth muscle cell migration
regulation of cell growth
regulation of lipid transport
Upregulated
Downregulated

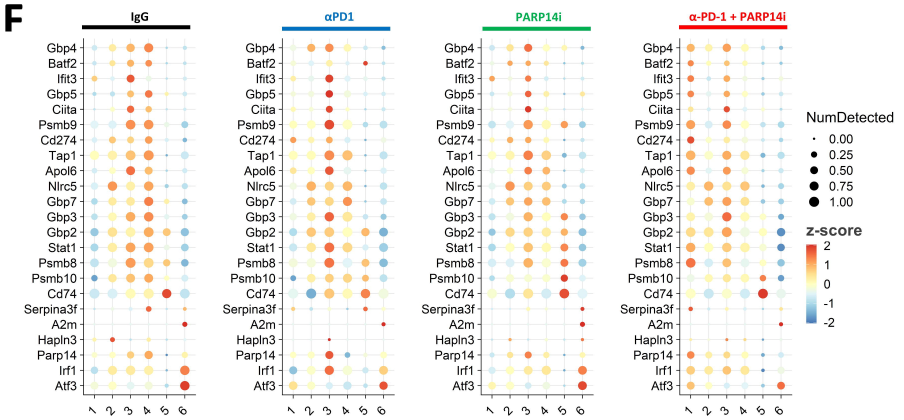
F
IgG
αPD1
PARP14i
α-PD-1 + PARP14i
Gbp4
Batf2
Ifit3
Gbp5
Ciita
Psmb9
Cd274
Tap1
Apol6
Nlrc5
Gbp7
Gbp3
Gbp2
Stat1
Psmb8
Psmb10
Cd74
Serpina3f
A2m
Hapln3
Parp14
Irf1
Atf3
NumDetected
0.00
0.25
0.50
0.75
1.00
z-score
2
1
0
-1
-2